Shape of plutons in crustal shear zones: A tectono-magmatic guide based on analogue models

Maria Michail[a], Michael Rudolf [b], Matthias Rosenau [b], Alberto Riva [a], Piero Gianolla [a], Massimo Coltorti [a,c]

[a] University of Ferrara, Department of Physics and Earth Sciences, Via Saragat 1, 44122 Ferrara, Italy

[b] Helmholtz Centre Potsdam, GFZ German Research Centre for Geosciences, Telegrafenberg, 14473 Potsdam, Germany

[c] National Institute of Geophysics and Volcanology, Palermo branch, Via Ugo la Malfa 153, 90125 Palermo, Italy

Correspondence: Matthias Rosenau (rosen@gfz-potsdam.de)

This manuscript has not yet undergone peer review and has been submitted to

Journal of Structural Geology

please cite as

Michail et al. (2021): Shape of plutons in crustal shear zones: A tectono-magmatic guide based on analogue models, earthArXiv, https://doi.org/10.31223/X5KG75

Shape of plutons in crustal shear zones: A tectono-magmatic guide based on analogue models

Maria Michail [a], Michael Rudolf [b], Matthias Rosenau [b], Alberto Riva [a], Piero Gianolla [a], Massimo Coltorti [a,c]

[a] University of Ferrara, Department of Physics and Earth Sciences, Via Saragat 1, 44122 Ferrara, Italy

[b] Helmholtz Centre Potsdam, GFZ German Research Centre for Geosciences, Telegrafenberg, 14473 Potsdam, Germany

[c] National Institute of Geophysics and Volcanology, Palermo branch, Via Ugo la Malfa 153, 90125 Palermo, Italy

Corresponding author: Maria Michail, email address: mchmra@unife.it, tel. 00393200486527

Keywords:

1. Analogue modelling;
2. Magma emplacement;
3. Strike-slip tectonics;
4. Transtension;
5. Pluton shape

21 **Abstract**

22 Plutons in crustal shear zones may exploit inherited structures, interfere with strain localizing or be
23 deformed passively. To constrain the relative timing of such tectono-magmatic constellations in
24 natural settings is not always straight-forward. We here present sandbox-type analogue model
25 experiments simulating magma emplacement into simple and transtensional crustal shear zones to
26 test the diagnostic potential of pluton shape with respect to timing and setting. Observations based
27 on surface deformation and intrusion shape exemplify the interplay between evolving and inherited
28 tectonic structures and magma uprising. We observe markedly asymmetric intrusions in association
29 with dikes reflecting the regional stresses, fault pattern and finite strain field. At the same time, the
30 presence of an intrusion modifies the tectonic evolution, but only transiently, resulting in short-lived
31 faults, reactivation and inversion. Diagnostic attributes include the pluton's aspect ratio, its
32 orientation and amplitude as well as dike association. Accordingly, syn-tectonic intrusions show the
33 highest pluton amplitudes and intermediate elongation oriented parallel to between Riedel shears in
34 simple shear, and compression in transtension. Post-tectonic intrusions are least elongated but
35 relatively high and exploit Riedel shears. Pre-tectonic intrusions are characterized by low amplitudes
36 and high aspect ratios parallel to the finite elongation direction. Intrusions in transtensional shear
37 zones are generally of lower amplitude than those in simple shear zones. Experimental results are
38 tested against observations from natural examples validating the diagnostic potential of pluton
39 shape for the timing and the tectonic setting of the emplacement.

40 **1 Introduction**

41 The spatial association of plutons and shear zones has long been recognized. Revealing their
42 temporal and spatial relation as a key to understand the mechanisms of tectono-magmatic
43 interaction, is a matter of research since. The interactions of tectonic and magmatic processes are
44 often ambiguous and hard to interpret (Paterson and Schmidt, 1999; Paterson and Tobisch, 1992).
45 It is generally recognised that both inherited structures and active faults represent key features in

46 crustal-scale magma transport and emplacement (Hutton, 1988; Hutton and Reavy 1992;
47 Vigneresse 1995; Román-Berdiel et al., 1997; Petford et al., 2000; Handy et al., 2001; Rosenberg,
48 2004; Corti et al., 2005; Galland et al., 2006; Galland et al., 2007b). Likewise, the presence of
49 magma in actively deforming crust may control fault localization and structural evolution (e.g.
50 Holohan et al., 2008; Dooley and Schreurs, 2012; Gomes et al., 2019). The delineated scenarios of
51 pre-, syn- and post-tectonic magmatism and the mechanisms involved remain poorly understood
52 taking also into account that gathering information from the field could be rather challenging. Beside
53 the limited outcrops in some areas, observations are, in most cases, restricted to the final stage of
54 magma emplacement which is often overprinted. In addition, the deformed upper crustal layers that
55 once hosted the magmatic chamber are in most cases subject to erosion and therefore missing from
56 the field. Consequently, the information on the incremental and finite deformation has to be inferred
57 with much effort from structural indicators and the processes taking place at depth must be
58 extrapolated (Vigneresse, 1995).

59 Modelling can help in overcoming some of the restrictions of field analysis and guide researchers
60 by identifying key observables and testing hypothesis. While all kinds of modelling have tackled
61 tectono-magmatic interaction, including analytical (e.g. Mandal and Chakraborty, 1990) and
62 numerical modelling (e.g. Burov et al., 2003), analogue models where used in particular for the
63 typically cross-scale and four-dimensional problems posed by tectono-magmatic processes (see
64 e.g. review by Galland et al., 2015). Amongst them, studies on syn-tectonic magma emplacement
65 prevail: a) in compressional settings (Galland et al., 2003, 2006, 2007; Mazzarini et al., 2010;
66 Montanari et al., 2010); b) in strike-slip settings (Román-Berdiel et al., 1997; Corti et al., 2005;
67 Mazzarini et al., 2010; Gomes et al., 2019); c) in transpressional settings (Benn et al., 1998); d) in
68 transtensional settings (Román-Berdiel et al., 2000; Corti et al., 2003) and finally e) in extensional
69 settings (Román-Berdiel et al., 1999; Mazzarini et al., 2010; Corti et al., 2003).

70 With a few exceptions (Holohan et al., 2008; Dooley and Schreurs, 2012; Gomes et al., 2019),
71 previous works were focused on syn-tectonic intrusion scenarios. However, little evidence exists

from analogue modelling regarding crustal shearing of pre- tectonic intrusion scenarios. Similarly, the post-tectonic intrusion system is very poorly studied, where exploitation of inherited structures from the uprising intrusion is still under debate. In this paper, we aim at closing this knowledge gap and test the diagnostic potential of pluton shape for relative timing with a new set of analogue model experiments simulating magma emplacement within the upper brittle crust rising from a basal ductile shear zone. We conduct a systematic series of magma emplacement scenarios in simple shear and transtensional regime (Fig. 1). To cover the full range of relative timing, we realize pre-tectonic, syn-tectonic and post-tectonic intrusion scenarios (Table 1).

In contrast to earlier analogue modelling studies with a similar goal (e.g. Román-Berdiel et al., 1997; Corti et al., 2005; Holohan et al., 2008; Mazzarini et al., 2010), we do not use a Riedel-type experiment with a linear velocity discontinuity at the base but a more realistic distributed basal shear zone (e.g. Dooley and Schreurs, 2012, and references therein). The viscous-weak body, in contrast to previous work (Holohan et al., 2008; Dooley and Schreurs, 2012; Gomes et al., 2019) is not lying parallel to the shear zone, but it is introduced vertically and in direct contact to the shear zone. In addition, in previous work the tectonic deformation of the magmatic chamber and the brittle crust, induced by the vertical upraising of the viscous – body, prior to and following the tectonic deformation, is not recorded. In the present study the magmatic chamber is not represented as an igneous pocket, but it is injected vertically, deforming this way the sand layers (no topography has been added in this study) before, during and after the tectonic deformation. In addition, the weak body appears with a fixed radius = 2cm, since the focus of the study is on the progressive interference with the brittle crust, for all emplacement scenarios. For this reason and in contrast to previous studies (Dooley and Schreurs, 2012; Zwaan and Schreurs, 2017) the intrusion geometry and its initial orientation (angular position) relative to the shear zone are not evaluated.

Using state of the art kinematic monitoring techniques (Digital Image correlation – DIC; Structure-from-Motion – SfM), the full 3D surface deformation over time (i.e. 4D deformation) and the final intrusion three-dimensional shapes are captured digitally at high resolution and accuracy. Based on

this experimental data set, which is openly available (Michail et al., 2020), we verify existing diagnostic features (e.g. pluton aspect ratio, orientation) and new attributes (pluton amplitude, dike association) of pluton shape and validate them against selected field examples. The presented models appear as a guide to the interpretation of necessarily incomplete and limited field observations. **(Figure 1 here)**

2 Methods and materials

2.1 Experimental setup

The experimental setup consists of two mobile plastic plates on a 1 by 1 m wide solid steel support platform. The mobile plates are moved by linear actuators, controlled by stepper motors, in opposite direction (Fig. 1). A 40-mm wide gap between the two 700 mm long and 7 mm thick mobile plates is filled with viscous material (silicone oil) to allow the formation of a distributed basal shear zone, similar to natural lower crustal shear zones (Fig. 1a-b). Two kinematically distinct experimental series, representing two different tectonic regimes, namely simple shear (reference model RS and models of group A; Fig. 1c,e) and transtension (reference model RT and models of group B; Fig. 1d,f) are presented (Table 1).

For the simple shear regime, the gap between the mobile plates is oriented parallel to the plates' motion (Fig. 1c,e*),* while in the transtensional configuration, they are oriented with an angle, α, of 15° (Fig. 1d). Relative plate velocity is fixed to 1 mm/min, for all experiments, which corresponds to a simple shear rate of $4.2*10^{-4}\ s^{-1}$ across the width of gap resulting in a final relative displacement of the two sides of the shear zone of 60 mm for all experiments. A low shear rate, together with a viscous fluid, rough inner edges of the mobile plates and polished and lubricated surface of the metal base, result in a well distributed deformation within the gap although minor localization of shear and extension at the shear zone boundaries is unavoidable. Simple shear and transtensional models are run under dextral and sinistral senses of shear, respectively, in order to ease their distinctness. **(Table 1 here)**

A 40-mm thick, sieved quartz sand layer representing the brittle upper crust (Fig. 1a-b) covers the mobile plates and the basal shear zone. On top of each mobile plate, fixed, motion-parallel sidebars confine the sand layer laterally and helps in model preparation (Fig. 1a,e). In the centre of the basal shear zone, a motor-controlled piston pushes silicone oil up through a pipe (with 40 mm diameter) placed beneath the experiment's foundation, to simulate the magma ascending from the lower crust into the upper-crustal shear zone (Fig. 1e-f). The piston moves at a velocity of 1 mm/min, which translates into an injection rate of 21 mm^3/s for all experiments (Table 1). All the experiments are performed under air-controlled ambient conditions (23°-25°C, 50% humidity).

2.2 Analogue materials

The viscous analogue material used for both the intrusion and the basal ductile layer is a silicone oil (Polydimethylsiloxane PDMS, G30M by K. Obermeier GmbH). It has a density of 965 kg m^{-3} and a Newtonian viscosity of 22.4 kPa s at laboratory strain rates below 10^{-2} s^{-1} (Rudolf et al., 2016; see Table 2). Earlier studies showed that similar material is a suitable analogue for ductile lower crust and, at reduced viscosity, for low density-high viscosity (i.e. granitic) magmas simulation (e.g. Román-Berdiel et al., 1997; Benn et al., 1998, 2000; Galland et al., 2015). We here use one material for simulating both the ductile lower crust and the magma in order to reduce rheological complexity but also due to practical reasons, i.e. to avoid gravitational flow of the material at the end of the experiment and to allow manual excavation of the ductile shear zone and the intrusion.

Sieved dry quartz-sand (G12) functions as brittle analogue of the upper crust. The sand is a well-sorted, well-rounded and fine-grained (<400 µm) sand of fluvial origin (Klinkmüller et al., 2016; Rosenau et al., 2018). When sieved, a bulk density $\rho \sim 1600$ kgm^{-3} is reached and the sand layer is characterized by internal friction coefficients μ of 0.69, 0.62, 0.55 (static, reactivated, sliding) and a cohesion *C* in the order of 50 - 110 Pa (Table 1). The localization behaviour of sand produces shear zones several grain diameters wide rather than idealized infinitely narrow faults. However, we here use the term "faults", to describe the small-scale shear zones, evolving in the analogue model because of the generally close dynamic similarity (Ritter et al., 2016). With the term "shear zone" in

contrast we refer to the regional deformation zone composed of several faults evolving on top of the basal ductile shear zone.

2.3 Scaling and Similarity

The experiments are scaled following the principles of geometric, kinematic and dynamic similarities to the natural prototype (Hubbert, 1937; Ramberg, 1981; Weijermars and Schmeling, 1986). Accordingly, for a brittle-viscous sandbox model under normal gravity, the stress scaling dictates the length and time scaling. In the pressure-dependent brittle regime and under normal gravity, the length scale L^* can be delineated from densities and cohesion in the model and prototype following the scaling law:

$$L^* = C^* / \rho^* \quad \text{(i)}$$

where the asterisks denote the model/prototype ratios known as the scaling factors (i.e. $C^* = C_{model}/C_{prototype}$). Inserting numbers for the scaling factors for density and cohesion of our brittle analogue rock material (C_{model} ~ 10-100 Pa, ρ_{model} = 1600 kg/m³) and typical upper crustal rocks ($C_{prototype}$ = 10 MPa, $\rho_{prototype}$ = 2600 kg/m³) yields a length scaling factor of L^* in the order of 0.6-6x10^{-6}, i.e. 1 cm in the model equals 0.6-6 km in nature (Table 2). Consequently, our model represents an intrusion into the upper 2-20 km thick crust. For our models, due to dimensional identity, the stress scale is also fixed by the choice of cohesion to $\sigma^* = 1\text{-}10\text{x}10^{-6}$.

In the strain-rate dependent viscous regime the time-scale T^* can be delineated, based on dimensional arguments, from the viscosities η in the model and in nature using the formerly set stress scale and following the scaling law

$$T^* = \eta^* / \sigma^*. \quad \text{(ii)}$$

With the viscosity of the silicone oil (η_{model} ~ 10^4 Pas) and considering a typical viscosity range for magma ($\eta_{prototype}$ = 10^4-10^{10} Pas), this scaling yields highly unsuitable laboratory time scales, that require running the experiments at even lower rates than in nature. This dilemma has already been noticed by Ramberg (1981) who stated that magma cannot be properly scaled because even the

most viscous (low water content, high silica) magma would require an analogue fluid, which is even less viscous than water and which does not exist. **(Table 2 here)**

To solve this dilemma, we here consider the rising magmatic body not as a homogenous melt with low viscosity but as a succession of rapid melt injections into the crust over millions of years. This is in accordance to the general view that plutons grow transiently over the Ma timescale fed by magma that transits through lower crustal shear zones episodically on the hundreds to thousands of years timescale (e.g. Handy et al., 2001, Patterson et al., 2011, Brown, 2013). The resulting magmatic system has therefore an effective bulk viscosity much higher than that of the individual melt components and which is more similar to ductile lower (quartz-feldspatic/andesitic) crust at typical regional tectonic strain rates ($\eta_{prototype} > 10^{20}$ Pas at $< 10^{-14} s^{-1}$, e.g. Shinevar et al., 2015). Such an alternative interpretation of the analogue model is not only consistent with modern views of episodic pluton growth but considers at the same time, though highly simplified, thermal aspects of the emplacement process (i.e. cooling and crystallization between injection episodes; Gomes et al., 2019). Following this reasoning and considering a Million-year time scale of pluton growth, we derive the time scale by relating the filling times of our model pluton (ca. 10^{-8} m³/s) to mean natural rates of 10^2 km³/Ma (e.g. Patterson et al., 2011). Accordingly, we arrive at $T^*=10^{-13}$ (1 second in the lab corresponds to ca. 30.000 years, Table 2). According to this timescale the applied velocity of 1 mm/min scales to ca. 0.5 mm/a in nature and a corresponding shear rate of ca. $10^{-17} s^{-1}$.

2.4 Monitoring and Analysis

We use state-of-the-art digital image correlation techniques for kinematic monitoring of the model surface deformation (Particle Image Velocimetry, PIV) and for deriving the surface topography and intrusion shape (Structure-from-Motion, SfM). All digital data generated in this study are published open access in Michail et al. (2020).

2.4.1 *Particle Image Velocimetry (PIV)*

A stereoscopic pair of charge-coupled device (CCD) cameras (11 MPx, 14bit, LaVision Imager ProX) monitor the model surface during the experimental run at a frequency of 0.3 Hz (Fig. 2a). Digital image correlation, using a least square minimization technique (as implemented in LaVision Davis 8), allows a quasi-continuous quantitative monitoring of the topographic evolution and surface deformation at high spatio-temporal resolution according to the principles of PIV (Adam et al., 2005). We derive 3D incremental and cumulative surface deformation pattern (i.e. velocity fields, strain fields and topography) at the sub-millimetre resolution.

From the surface velocity field, we produce surface strain maps which show the incremental shear strain E_{xy} (the unit of which is millistrain, mS), highlighting active faults and their kinematics. Positive values (red colors in all Figures) indicate a clockwise rotation or dextral shear sense and negative values (blue colors in all Figures) indicate anti-clockwise rotation or sinistral shear. The final shear strain is computed as the cumulative (or finite) displacement field indicating the relative importance of individual faults in accommodating deformation over the full experimental range.

2.4.2 *Structure-from-Motion (SfM)*

To obtain the 3D model reconstruction of the final topography (digital elevation model, DEM) and the final intrusion shape (digital intrusion model, DIM) at high resolution we rely on the Structure-from-motion (SfM) technique (Westoby et al., 2012) using digital images taken at the end of every experiment with a customer grade DSLR camera (NIKON D80, 10 MPx). Images including perspective views of both the final model surface and the model intrusion after excavation taken from various angles are used for the 3D model reconstruction achieved by using Agisoft PhotoScan (Professional Edition). For visualization coloured DIM-contours have been extracted from the models.

The intrusion's geometry (pluton shape) is quantified using various dimensionless parameters derived from the DIM:

First, its normalized amplitude

$$A_{intrusion} = H_{intrusion} / H_{sand\ layer} \quad \text{(iii)}$$

where $H_{intrusion}$ is the intrusion height above the initial surface of the ductile layer and $H_{sand\ layer}$ is the thickness of the sand layer (i.e. 40 mm). Second, the aspect ratio

$$r = L/W \quad \text{(iv)}$$

calculated based on the length L and width W of the ellipse that fits to the DIM perimeter at a given contour level.

Third, the orientation of the intrusion, that is described by Θ, defined as the angle between the long axis L of the fitted ellipse and the strike of the basal shear zone. Θ is counted counter clockwise. Aspect ratio and angle of intrusion are derived for each contour level allowing the analysis of the shape as a function of height.

3 Experimental results

Nine experiments in total are presented and discussed in the following sections (Table 1): i) three reference experiments (Group R); ii) three models of intrusion under (dextral) simple shear (Group A) and iii) three models of intrusion under (sinistral) transtension (Group B). Pre-, syn and post-tectonic intrusion scenarios are presented for the Groups A and B. Group R consists of a static intrusion without applied shear (R0), a simple shear (RS) and a transtensional experiment (RT), both without intrusion. Rates of intrusion and deformation are kept constant in all experiments as well as the thickness of the brittle layer.

3.1 Reference models (Group R)

The surface evolution of the reference experiments, namely the static intrusion model (R0, Fig. 2a-c), the simple shear model (RS, Fig. 2d-f) and the transtension model (RT, Fig. 2g-i) is summarised in Fig. 2. In the R0 model, a circular sand dome starts to form above the intrusion as soon as the

injection has started (V_{inj} = 3.2 ml; Fig. 2a). Gradually, the sand layer forms an elongated rectangular domal uplift preserved until the latest intrusion stage, bound by lateral reverse faults, parallel to the basal ductile layer (Fig. 2b-c). The uplift rate decreases with time. **(Figure 2 here)**

For the reference experiments under simple shear (RS) and transtensional (RT) deformation the surface evolution shows a typical sequence of structures consistent with previous studies using a distributed basal shear zone and dry sand layers (Román-Berdiel et al., 1997; Corti et al., 2005; Dooley and Schreurs, 2012). In the very early evolution stage of the RS model (d_{rel} = 5.0mm) a diffuse belt starts to form above the basal ductile shear zone (Fig. 2d). With increasing displacement, early en-échelon synthetic Riedel shears (R) develop with a trend of ~20° to the trace of the basal shear zone (d_{rel} = 16.1 mm; Fig. 2e). Lower-angle synthetic shears develop between the overlapping R shears, having a strike of ~15° (Fig. 2e). The final deformation surface pattern (d_{rel} = 38.3 mm) is characterised by the formation of an active and continuous master fault (MF), as a result of the linkage of the individual early shear structures, parallel to the basal shear zone, along which less active anastomosing minor faults which define shear lenses and pop-up structures (d_{rel} = 38.3 mm; Fig. 2f). The final surface width of the shear zone (ca. 50 mm) is larger than the basal shear zone (40 mm; Fig. 2f).

The transtensional reference experiment (RT) shows an early evolutionary history similar to the simple shear experiment with the formation of a diffuse shear zone above the basal ductile shear zone (Fig. 2g-i). Linkage of early right-stepping and overlapping R shears occur along lower angle structures (Y, P shears) causing a deformation localization in the central part and forming a through-going master fault from early on (d= 11.1 mm; Fig. 2g-h). During the final stage, the deformation partitions between lateral faults and fault-bounded rhomboidal basin structures (Fig. 2i). In this stage, the pull-apart basin structure is cut short by strike-slip faults that continue to propagate towards the dominating parallel boundary faults. This results in lengthening and narrowing of the pull-apart basin in a direction parallel to the displacement vector. The final surface width of the shear zone is larger (ca. 60 mm) than the basal shear zone (44.4 mm; Fig. 2i).

3.2 Simple shear intrusion models (Group A)

3.2.1 Effect of intrusion on fault pattern

The three models presented in this group show the evolution of deformation with the presence of analogue magma injection that predates (A1, pre-tectonic model), coincides (A2, syn-tectonic model) and post-dates (A3 post-tectonic model) the applied simple shear deformation. Our observations focus on the interactions taking place between faulting and intrusion and how they affect the fault pattern evolution and the final intrusion geometry.

The pre-tectonic intrusion experiment, model A1 (Fig. 3), consists of two parts: during the first half of the experiment, static intrusion takes place (V_{inj} = 37.3 ml) causing a domal uplift (Δh_{init} = 7 mm, Fig. 3a) as described for the R0 model (Fig. 2a-c). In the second half of the experiment, following the static intrusion, dextral shearing is applied. Accordingly, in the early intrusion stage there is no obvious fault formation (Fig. 3a). Once shearing started diffuse deformation occur in a spindle-like surface area (d_{rel} = 11.4; Fig. 3b) forming a wider shear domain bound by transpressional faults. At a later stage of shearing (d_{rel} = 22.2 mm; Fig. 3c) a system of strike-slip faults consisting of two lateral and one central fault is cutting through the uplifted domain. The finite fault pattern (Fig. 3d-f) is, in contrast to the model RS, characterized by a wider strike-slip system encompassing the intrusion area and external transpressional faults which have been active mainly during early stages of deformation. **(Figure 3 here)**

The fault pattern in the syn-tectonic intrusion experiment, model A2 (Fig. 4), initially evolves in a similar fashion as in model A1. In the early deformational stage (d_{rel} = 3.9mm; V_{inj} = 4.9ml; Fig. 4a) a diffuse spindle-like shear zone occurs encompassing the uplifting centre. With ongoing shearing and intrusion (d_{rel} = 6.7mm; V_{inj} = 4.9ml; Fig. 4b) transpressional faults localize at the periphery of the spindle-like area embracing the intrusion domain as well as Riedel shear in the centre. In the late stage (d_{rel} = 27.8mm; V_{inj} = 35.0ml; Fig. 4c) deformation localizes into a narrow strike-slip fault system cutting the intrusion area. This set of parallel, locally transtensional faults cause the depressing of the uplifted central domain (Fig. 4e). The finite fault pattern (Fig. 4d-f) shares

297 characters of the reference model RS (a central strike-slip fault system; Fig. 2d-f) and the pre-
298 tectonic model A1 (early stage transpressional faults swinging around the intrusion area; Fig. 3b).
299 **(Figure 4 here)**

300 The post-tectonic experiment, model A3 (Fig. 5) consists again of two parts: In the first half, the
301 experiment follows according to the observations documented for the RS model (d_{rel} = 30mm; Fig.
302 2d-f) resulting in a system of strike-slip faults (Fig. 5a) at the start of intrusion. In the second half of
303 the experiment, static intrusion causes formation of new lateral faults (in the "south" of the intrusion)
304 but also the reactivation of inherited, lateral faults (in the "north" of the intrusion; V_{inj} = 12.6-32.2ml;
305 Fig. 5b-c). Importantly, active faults in opposite corners of the intrusion show a synthetic sense
306 including dextral and sinistral shear (Fig. 5b-c). Consequently, dextral displacement across inherited
307 faults acquired in the first half of the experiment is now partly inverted. The finite fault pattern (Fig.
308 5d-f) is a composite of partly re-activated strike-slip faults similar to the reference model R0 (Fig.
309 2h-i) and new reverse faults embracing a central domal uplift. **(Figure 5 here)**

310 *3.2.2 Effect of deformation on intrusion shape*

311 Among the three emplacement scenarios there is a significant variation regarding the final
312 geometrical features of the intrusion described by the intrusion's absolute height (H) and normalized
313 amplitude (A), its aspect ratio (r = length/width) and the orientation of its long axis (angle θ). The
314 intrusion models appear strongly deformed and asymmetric, revealing the tectonic impact during
315 their emplacement, and have a systematic generic relation to the regional stress and finite strain
316 fields (Fig. 6).

317 The intrusion of Model A1 (pre-tectonic, Fig. 6a-d), which has been passively deformed is
318 characterized by low height and amplitude (H_{A1} = 15 mm, A_{A1} = 0.38), compared to intrusions from
319 other scenarios. Its asymmetry is related to displacement along the crosscutting faults developing
320 late in the experiment. The lower part of the intrusion represented e.g. by the contour level c_1 = 3mm
321 shows a relatively high aspect ratio (r_1 = 2.7) with the long axis of the intrusion forming a low angle
322 of θ_1 = 12° to the shear zone. At higher contour levels the intrusion progressively elongates (r>3)

and rotates antithetic (i.e. anticlockwise) with respect to the dextral simple shear (e.g. θ_2 = 34° at c_2 =12mm) becoming subparallel to the elongation direction of the finite strain tensor (Fig. 7; A.2). The intrusion roof is sculpted by one central and two lateral dikes that represent silicone oil intruding upwards along the master fault (MF) and the lateral faults, obviously during the post-intrusion stage of the experiment. **(Figure 6 here)**

The intrusion Model A2 (syn-tectonic, Fig. 6e-h) is characterized by an acute roof resulting in a significant height and amplitude (H_{A2} = 24mm; A_{A2} = 0.6; Fig. 6e-f) compared to intrusions from other scenarios. It shows a strong asymmetric wing shape with opposing orientation to the intrusion model A1. At lower levels, the intrusion has a high aspect ratio (e.g. r_1 = 2.5) with the long axis almost parallel to the shear zone (θ_1 = 1°). Upwards, the intrusion progressively rotates synthetically into the orientation of Riedel shears (e.g. θ_2 = -10° at c_2 = 20mm) while keeping its aspect ratio rather constant (Fig. 7; A.3). Lateral dikes flank the central upheaval with all of them exploiting faults formed during intrusion. The wing shape of the intrusion in association with scissor tailed and offset apophyses appears unique to this scenario. **(Figure 7 here)**

The intrusion Model A3 (post-tectonic, Fig. 6 i-l) is characterized by a more domal shape with intermediate height and amplitude (H_{A3} = 22 mm; A_{A3} = 0.55). It appears sub-circular to gently elongated ($r<2$) and largely subparallel to the shear zone with no systematic change of aspect ratio and orientation with height (Fig. 7; A.4). The roof is rounded and sculpted by a central dike (r_2 = 1.9 at c_2 = 19mm) and two lateral dikes exploiting inherited structures (Fig. 6i-j).

3.3 Transtensional intrusion models (Group B)

3.3.1 Effect of intrusion on fault evolution

Transtensional intrusion experiments demonstrate, similarly to Group A, ongoing interactions developing between the intrusion and the fault pattern evolution for all three scenarios.

In the first half of the pre-tectonic intrusion experiment, model B1, static intrusion takes place (V_{inj} = 37.7 ml), deforming the initially flat topography and causing a domal surface uplift (Δh_{init} = 7 mm; Fig. 8a) above the centre. In the second half of the experiment, transtension is applied and a diffuse spindle-like shear zone occurs (d_{rel} = 5.6 mm; Fig. 8b) similar as in the pre-tectonic simple shear model A1. With ongoing transtension, lateral oblique normal faults and oblique Riedel shears localize deformation (d_{rel} = 16.7 mm; Fig. 8c) causing subsidence along the shear zone. The initial central dome is crosscut by a fault system (P and Y-shears) that links the "northern" and "southern" boundary faults, which remain active until the end of the experiment (Fig. 8c-f). Similar to the reference model (RT, Fig. 2g-i), Riedels form an en-enchelon array of oblique normal faults within the basin (Fig. 8d). The finite deformation pattern of the surface is characterised by a well-defined elongated pull-apart basin (Fig. 8d-f). The domal uplift, caused by the initial intrusion, is overprinted and appears as a remaining gentle uplift in the centre (Fig. 8e). Notably, the topographic expression of the pre-tectonic intrusion is much less than in the corresponding simple shear model A1 (Fig. 3e). **(Figure 8 here)**

The early stage of the syn-tectonic intrusion experiment, model B2, is characterized by diffuse shear and Riedel shear formation (d_{rel} = 1.2 mm; V_{inj} = 1.5 ml; Fig. 9a). At an intermediate stage (d_{rel} = 8.3 mm; V_{inj} = 10.5 ml) and along with subsidence, the linkage of these Riedel shears form a dominant fault zone that diverges from the strike of the basal shear zone to form a releasing stepover centred on the intrusion domain (Fig. 9b). At a late stage (d_{rel} = 16.7; V_{inj} = 21; Fig. 9c) oblique normal faults bound the outer basin margins and curve towards the centre (Fig. 9c). As the master fault continues to propagate, it crosscuts and deforms the evolving basin. The finite fault pattern (Fig. 9d-e) is, in contrast to the reference model (RT, Fig. 2g-i), characterised by a more segmented and curved faults bounding the elongate basin with the deep central graben flanked by horst blocks. **(Figure 9 here)**

The post-tectonic intrusion experiment, model B3 (Fig. 10), is divided again into two parts: the first transtension as described for model RT model (Fig. 2g-i), resulting in a fault-controlled, spindle-

shaped pull-apart basin (d_{rel} = 30mm; Fig. 10a, d). Then static intrusion (V_{inj} = 13 ml) starts to form a domal uplift, triggering the re-activation of the pre-existing faults (Fig. 10b). Similarly as observed in model A3, inherited faults are reactivated and partly inverted (Fig. 10b-c). The master fault is re-activated in sinistral sense while dextral displacement occurs along inverted boundary faults (V_{inj} = 18.6; Fig. 10c). The finite topography (Fig. 10d-e) directly reflects the intrusion at depth within the basin system (Fig. 10d-e). **(Figure 10 here)**

3.3.2 Effect of deformation on intrusion geometry

The intrusion Model B1 (pre-tectonic, Fig. 11a-d) is like the corresponding Model A1 characterized by low height and amplitude and enhanced by post-emplacement flattening in the transtensional regime (H_{B1} = 5 mm; A_{B1} = 0.13). The intrusion's aspect ratio shows characteristic high values but with no systematic change with height (Fig. 12; A.5), varying from 1.8 at c_1 = 1mm (Fig. 11c) to 1.9 at c_2 = 3mm (Fig. 11d). The orientation of the intrusion, similar to A1, rotates from the base to the top antithetic (i.e. clockwise) with respect to the sinistral sense of transtensional shear to become subparallel to the finite strain tensor (e.g. θ_2 = 42°; Fig. 12). The intrusion's flat roof is sculpted by lateral dikes exploiting faults developing during the post-emplacement deformation. **(Figure 11 here)**

The intrusion Model B2 (syn-tectonic; Fig. 11e-h) similarly to model A2 is characterised by an acute shape (H_{B2} = 22 mm; A_{B2} = 0.6). The intrusion's base shows an intermediate aspect ratio of r_1 = 1.7 with the long axis subparallel to the shear zone boundary (e.g. θ_1 = -10°; Fig. 11g). Upwards, the intrusion rotates synthetically towards the maximum horizontal stress orientation, σ_{Hmax} (Fig.11h; Fig. 12; A.6). This model bears a smooth roof top and lateral dikes flanking the central upheaval. The asymmetric wing shape marked by a scissor tail apophyses that trails behind the intrusion are similarly observed for model A2 (Fig. 6e-h). **(Figure 12 here)**

Finally, the intrusion Model B3 (post-tectonic, 11j-l) is a sub-circular to slightly elongated intrusion of domal shape (H_{B3} = 20 mm; A_{B3} = 0.5). At lower contour levels, the intrusion shows an aspect

ratio of r_1 = 1.4 with the long axis parallel to the shear zone like model A3 (Fig. 11k; Fig. 12; A.7). The intrusion has an asymmetric roof of carrying a central dike (r_2 = 1.7 at c_2 = 18mm) and two lateral dikes (Fig.11l). The latter exploits inherited faults (θ_2 = -11°; Fig. 7).

4 Discussion of experimental results

We here present sandbox-type analogue model experiments simulating magma emplacement into simple and transtensional crustal shear zones to test the diagnostic potential of the finite pluton shape with respect to timing and setting of its emplacement. Observations based on surface deformation and intrusion shape illustrate strong interactions between evolving and inherited tectonic structures and magma uprising, plus constitute an important contribution in defining the diagnostic potential of pluton shape for the timing and the tectonic setting of the emplacement.

4.1 Synthesis and comparison of experimental results

4.1.1 Controlling parameters on pluton emplacement

In this study the timing of the magmatic emplacement with respect to the regional tectonic deformation is inferred as a controlling parameter on the finite pluton geometry and emplacement mode. Parallelly, the shape of the produced intrusions, based on the timing of their emplacement, is suggested as an effective diagnostic feature. Notably, the findings of this work extend the results of previous studies which observed and described experiments restricted under reference conditions (static, shear deformation) and processes of syn-tectonic magmatic emplacement.

Based on our observations, the pluton emplacement is directly controlled by the syn-active evolving faults, for both groups in pre- and syn-tectonic scenarios. At the same time, strain localization on the weak body influences the upward fault propagation. Post-tectonic models are influenced and overprinted by the boundary conditions and indirectly by the inherited fault structures during their emplacement. According to our observations and in agreement with previous related studies (Román-Berdiel et al., 1997; 2000; Corti et al., 2005) local interactions between on-going fault propagation and magma uprising induce asymmetric intrusion shapes. In addition, the thickness

ratio between the brittle and ductile band, influence the interactions between the intrusive analogue magma and the developing model surface fault pattern. In our case, the ratio between the ductile band (7mm) and the brittle layer thickness (40mm) is fixed at 0.175. This ratio allows us to observe the overburden deformation without the fault pattern being completely overprinted by deformations induced by piercement of the surface.

Román-Berdiel et al. (2000) pointed out the importance of the divergence angle, α, in deformation styles of both surface and magma models, suggesting that for low values (i.e. α = 15°) under transtension the fault pattern is similar to pure simple shear kinematics, therefore resulting in similar geometries for the syn-tectonic intrusions. The fault structures observed in the reference experiments (RS and RT), during which no intrusion takes place, are very similar to those described in previous experiments (e.g. Tchalenko, 1970; Wilcox et al., 1973; Naylor et al., 1986). Moreover, for α < 30°, the deformation is mainly located in the central part of the model and the localization of brittle deformation is very high (Román-Berdiel et al., 1999; 2000).

Previous studies have shown that variations in the displacement velocity and the intrusion rate control the final geometry and orientation of the syn-tectonic magmatic body emplaced in the upper crustal layer (Román-Berdiel et al., 1997; Corti et al., 2005). According to these studies, high horizontal-displacement or low intrusion rates resulted in normal pluton asymmetry with the pluton's long axis parallelising the velocity discontinuity (VD) zone, whereas low horizontal-displacement or high intrusion rates, generated plutons with reverse asymmetry (magmatic emplacement controlled by tensional faults). In this study the variation of the ratio between tectonic displacement rate and intrusion rate is constant. However, by varying the time of emplacement we also captured observations on the pluton's asymmetry. Both pre-tectonic models show normal pluton asymmetry, with the long pluton axis forming with the shear zone angles of θ = 28° (Model A1, Fig. 6c-d) and θ = 42° (Model B1, Fig. 11c-d) and stretched to the extension direction. In the contrary, syn- and post-tectonic models, from both experimental groups, show reverse asymmetry with their long axis stretched to the compression direction, forming low angles with the shear zone (Fig. 6, Fig. 11f,i).

4.1.2 Interactions between deformation and pluton emplacement

The significant geometrical differences of the finite intrusions' shape observed among the emplacement scenarios (Fig. 6, Fig. 11) reveal strong interactions between deformation and intrusion emplacement (Román-Berdiel et al., 1997; Corti et al., 2005; Galland et al., 2007a; Montanari et al., 2010; Gomes et al., 2019). Our experimental results, in both simple and transtensional shear settings, show that pre- and syn-tectonic scenarios produce more elongated and fault-controlled intrusions in comparison to the less deformed post-tectonic intrusions characterised by low aspect ratios. The presence of intrusion causes regional surface uplift above the injection point and interferes with the fault structure evolution during their propagation. Regarding the reference models, with no intrusion presence, fault-controlled pull-apart basin system and of high subsidence rate occur for the transtensional group. The simple shear deformation results in a low angle main deformed linear zone formed by low angle shears and anastomosing shear lenses. Exception to this topography is Model A2 that resulted in narrow pull-apart system divided and displaced by the MF (Fig. 4e).

In accordance to the study of Gomes et al. (2019), this study illustrates that the shear zone deformation can be significantly modified by rheological heterogeneities by looking at the shear zone perturbation effect arising from passive (pre-tectonic) viscous-weak bodies. The pre-tectonic plutons, A1 and B1, with the gradual evolution of the post-emplacement shearing start to accumulate strain deformation in a ductile manner acquiring a sigmoidal (initially circular) shape of high aspect ratio and the lowest amplitude among all models (Fig. 6a-d, Fig. 11 a-d). This is very well shown from the shape analysis, where the lower levels of these intrusions are subparallel to the shear zone while the highest levels follow the finite stretching direction (Fig. 6c-d, Fig. 11c-d). The surface structures observed only for this model are acting separately over the domal uplift and not as one master fault (Fig. 3f). These above results seem compatible with the inferred observation on caldera collapse modelling and the case of strike-slip deformation of brittle layer containing a passive magmatic chamber (Holohan et al., 2008), where the magmatic chamber showed a NE-SW pluton

476 axis orientation, stretched approximately parallel to the extensional direction (in accordance to
477 current study Models A1 and B1). The limitation of pre-tectonic models, by the fault structures
478 developing subparallel to the boundary of the shear zone is an observation that is only attributed to
479 the variations on the overburden thickness (Román-Berdiel et al.,1997). The presence of the weak
480 body delays the upward propagation of the synthetic Riedel shears and results in a wider shear
481 zone, in respect to its reference model (Fig. 2f, Fig. 3f). Fact that is inferred from the deformational
482 response and the delay of the shear zone formation on the brittle surface, in comparison to the
483 reference models (Fig. 2, Fig. 3, Fig.8).

484 In the case of the syn-tectonic intrusions, direct and strong interactions are developing among fault
485 propagation and magma ascent. Faults control and confine the emplacement of the intrusions,
486 resulting in narrow and acute pluton shape that follows the highly active master fault (e.g. Román-
487 Berdiel et al., 1997; Corti et al., 2005; Mazzarini et al., 2010). Syn-tectonic models in simple shear
488 deformation show the highest pluton amplitude among all models (A_{A2} = 0.6; Table 3). From the
489 shape analysis of the excavated intrusions is inferred local fault control on the intrusions' boundaries
490 and orientation. Models A2 and B2, are initially orientated subparallel to the shear zone (intrusions'
491 lower level), with very low long axis angles. The deviation of their deformational is registered at their
492 highest levels when Model A2 seems to follow the Riedel orientation (Fig. 6h) while Model B2 is
493 oriented subparallel to S_{Hmax}.

494 The post-tectonic intrusions, Models A3 and B3, ascend without being exposed to the stress field,
495 besides the push from below during their ascent. The shape analysis reveals a characteristic
496 subcircular intrusion of an intermediate amplitude (A_{A3} = 0.55; A_{B1} = 0.5; Table 3) and with an
497 analogous axis orientation to the syn-tectonic models (Fig. 6k-l, Fig. 11k-l). Only from the strain
498 analyses it is inferred that in both settings, the uprising intrusions interferes and reactivates the pre-
499 existing brittle structures (Fig. 5c, Fig. 10c).

500 As a second order feature, the dike system overprinting the intrusions, is observed and analysed
501 upon excavation. Diking occurs locally and along fault structures and for all models, is developing

either on the intrusion's flat roof top, as in the cases of pre- and post-tectonic emplacement models (Fig. 6a-b; i-j, Fig. 11a-b; i-j) or as a form of a sheared tail intrusion's extension, as in the case of the syn-tectonic A2 and B2 Models (Fig. 6e-f, Fig 11e-f).

Our models have shown that the pluton's geometry functions as an excellent first order discriminator for the timing of the intrusion with respect to tectonic activity. In addition, this study offers information on the surface deformation, often limited during field work due to the occurrence of natural (e.g. erosion) and tectono-magmatic processes. The diagnostic attributions are summarized in Table 3. **(Table 3 here)**

4.2 Model boundary conditions, simplifications and limitations

Effect of the basal ductile shear zone on the emplacement process

We use a ductile homogenous shear zone as a basal kinematic boundary condition, which mimics a natural mid-crustal shear zone. Apart from distributing deformation, the ductile material also influences the emplacement mechanisms as reported in previous studies (Román-Berdiel et al., 1997, 2000; Corti et al., 2005; Montanari et al., 2010; Mazzarini et al., 2010). In those models, the presence of a widespread ductile layer is a pre-requisite to allow lateral flow and emplacement in laccolith style. It is suggested that for the syn-intrusive deformation the rheological stratification caused a deeper level of emplacement with respect to purely brittle models and thus controls the timing of magma emplacement. For our experiments, instead of a widespread ductile layer, we introduced a basal ductile band. Intrusions are allowed within the ductile band and above the fixed injection tube. The effects described previously is similarly active in our setup with lateral intrusion aided by the ductile material.

Ignoring thermal and strain-rate dependent effects on rheology.

The deformation in our experiments was accomplished by a quasi-stationary rheology including temperature- and strain rate-insensitive brittle and Newtonian viscous materials. Our modelling faces therefore some limitations regarding rheological principals (Corti et al., 2003). Magma cooling

527 is considered in simplified way by choosing a relatively high viscosity of the model magma (see
528 chapter on scaling and similarity 2.3). Thermal effects caused by the intrusion-related heating on
529 the rheology of the crustal rocks were not taken into consideration for our modelling as for all other
530 models of this type (Román-Berdiel et al., 1997; Corti et al., 2003; Galland et al., 2003, 2006, 2007;
531 Montanari et al., 2010; Mazzarini et al., 2010). At shallow crustal levels as those targeted here,
532 intrusion of rather small amounts of hot material into cold crust has likely a minor effect on the
533 geotherm and thereby on the rheology in general. However, the brittle-ductile transition might be
534 more sensitive to even small fluctuations in the geotherm caused by episodic heat advection by
535 veining and long-term emplacement of the intrusion (e.g. Handy and Streit, 1999; Brown, 2013). Any
536 modification of the rheology around the base of our models including temperature and strain-rate
537 dependent viscosity changes or even switches in the dominant deformation mechanisms (and
538 thereby the geometry of the brittle-viscous transition) is however beyond the scope of this modelling
539 approach. While we consider this drawback of the method more significant at a small scale,
540 numerical modelling might help in verifying the validity of our more stationary approach on a more
541 regional scale.

542 *What drives deformation in the model versus nature?*

543 In our experiments model magma is rising due to two different forces: pressure applied externally
544 and internal buoyancy forces (e.g. Ribe and Davaille, 2013; Wouter et al., 2016). Though qualitative
545 similar mechanisms act in nature the dynamic similarity is hard to verify. Pressure in the model is
546 controlled by the applied intrusion rate and decreases over an experimental run as the intrusion rate
547 is kept constant while the volumetric fraction added to the growing intrusion decreases with 1/t
548 systematically. Given the geometric and kinematic similarities described above we suspect a
549 realistic de-pressurization scenario in the model. However, given the lack of quantitative
550 observations in nature a conclusion remains elusive. Buoyancy in the model is likely more important
551 than in nature because the density ratio between PDMS and sand is low (1:1.7) while it may be
552 closer to equality (1:1) or even >1 (negatively buoyant) in nature, depending on magma composition.

As we observe silicone dikes intruding the overburden in a similar fashion as in nature (e.g. roof dikes, see below), we suspect however, that buoyancy driven intrusion (i.e. diapirism) mimics residual melt injection driven by local pressure anomalies in the prototype.

4.3 Comparison with nature

Analogue modelling may be characterised by strong limitations and simplifications, mainly related to the inability to reproducing natural thermal and rheological conditions. In addition, limitations on direct comparison among natural and analogue models may be due to restricted exposure of plutons. From our observations, the spatial and temporal relationships between emplacement-related structures and intrusion vary with the level of the exposure. Analogue modelling studies have managed to reproduce models with similar geometrical features of the plutons in the upper crustal levels, for different tectonic settings, supporting the field evidences on tectonic control during pluton emplacement (Castro, 1987; Hutton, 1988) and testifying the reliability of this modelling approach (Román-Berdiel et al., 1997, 2000; Galland et al., 2003; Corti et al., 2005; Gomes et al., 2019).

The current analogue modelling approach provides new insights on the reliability of the finite pluton shape as a diagnostic key-feature for constraining the temporal timing (pre-, syn- and post-tectonic) and spatial conditions (tectonic setting) of the shallow crustal level emplacement. To validate our experimental observables, we test them along with some second-order attributes against six cases of well-defined natural examples, emplaced in simple shear and transtensional zones (Fig.13).

4.3.1 Natural examples of intrusions along simple shear zones

The pre-tectonic Teixeira Pluton (Fig. 13a,d) – This elongated ENE-trending batholith (80 km x 25 km) is situated in NE Brazil and within a zone that is defined by the E-trending Patos, the So Josèdos Cordeiros and the Juru shear zones (Fig.13a). The pre-tectonic Teixeira batholith is a leucocratic granite to quartz-syenite in composition that shows a crystallization age of 591± 5 Ma (Zircon U/Pb). The batholith fabrics, determined by anisotropy of magnetic susceptibility (AMS) and mineral shape preferred orientation, support a pre-transcurrent batholith emplacement scenario (Archanjo et al.,

578 2008). This natural example carries similar features to the pre-tectonic Model A1 of this study (Fig.
579 6a-d). The pluton is characterised by high aspect ratio (L/W > 5), with the long axis orientated
580 subparallel to the extensional direction, forming an angle of α = 15°. The Teixeira pluton, on map
581 view, is elongated in a northeast-southwest direction, consistent with the dextral pure strike-slip
582 motion (Fig.13a).

583 Another natural example with similar characteristics to the pre-tectonic model A1 is the granitic
584 Tazenakht Pluton in Morocco. The pluton's deformation follows its emplacement within a left lateral
585 strike slip fault, running along its northern side (Ennih and Liegeois, 2001; Gasquet et al., 2008).
586 The boundaries developing between the fault structure and the intrusion boundaries are sharp. The
587 pluton was probably subject to a minor rotation during the deformational post-intrusion event. This
588 natural example is characterised by high axis ratio ratio (L/W = 1.6) and the pluton's long axis forms
589 an angle of α = 29° with the shear zone. The local presence of dykes and the geometrical features
590 of the pluton are similar to those observed for the Model A1.

591 *The syn-tectonic Cabeza de Araya Pluton* (Fig. 13b,e) –The plutons of the Central Extremadura
592 batholith in the Iberian Massif (Fernández and Castro, 1999) is a natural example of syn-tectonic
593 plutonism. This natural example was imposed to tectonic deformation during its emplacement,
594 triggered by a right-lateral shear zone (Vigneresse and Bouchez, 1997; Fernández and Castro,
595 1999; Corti et al., 2005). The emplacement mode of the pluton is coeval with the dextral regional
596 shear zone (Castro, 1985). The pluton shows an aspect ratio of L/W = 2.7, with the long axis forming
597 an angle of α = -45° parallel to the compression direction (NW-SE direction, Fig. 13b). Similarly, an
598 intermediate axis ratio is observed for the syn-tectonic Model A2 (r = 2.5; Fig. 6g, h). The model's
599 long axis that corresponds to the higher contour levels is orientated with the angle of (θ = -10°),
600 making this natural model a prototype for this emplacement scenario. In addition to this, there are
601 also other important natural examples of syn-tectonic intrusion emplacement scenarios that shows
602 similarities to our observations: 1) *Karawanken pluton* (Visonà and Zanferrari, 2000; Rosenberg,

603 2004); 2) *The Lizio pluton* (Román-Berdiel et al., 1997; Fernandez and Castro, 1999; Corti et al.,
604 2005); 3) *Cases of Syn-tectonic magmatism along the Periadriatic Fault System* (Rosenberg, 2004).

605 *The post-tectonic Vila Pouca de Aguiar pluton* (Fig. 13c,f) – This is a natural example of a post-
606 tectonic granitic intrusion that is emplaced after the main left-lateral shear phase event (Sant'Ovaia
607 et al., 2000). It is suggested that the first to be emplaced and the least evolved granite type (Vila
608 Pouca de Aguiar Granite) upwelled from the local, NE-trending fault-zone, acting as a dike, and
609 formed a thin sill where NE-directed magma flow was dominant. In this case, the pre-existing
610 features exert a major role during emplacement leading to the roughly alignment of the intrusion
611 with the shear zone (α = -4°; Fig.13f), with the pluton axis parallel to the compression direction. Even
612 if the pre-tectonic group generated intrusions with the lowest aspect ratios (r < 1.5; Fig. 7), the
613 intrusion ellipses corresponding to higher contour levels resulted in a similar aspect ratio (r = 1.9)
614 and elongated shape to the *Vila Pouca de Aguiar* pluton (Fig. 6l).

615 Another characteristic natural example of post-tectonic emplacement is the Águas Frias (AF) pluton
616 (Martins et al., 2009; Fig. 13c). This post-tectonic granitic pluton is situated NE from the Vila Pouca
617 de Aguiar pluton, occupying an area of 30 km^2 and is associated with Penacova-Régua-Verin fault
618 (PRVF) that belongs to the NNE-trending brittle fault system. Its emplacement is fed through a deep
619 conduit located at the centre of the pluton. VPA and AF plutons show similar in mineralogical,
620 chronological and magnetic features. Their feeding zones are located within the NNE-SSW
621 Penacova-Régua -Verin Fault. **(Figure 13 here)**

622 *4.3.2 Natural examples for intrusion into transtensional shear zones*

623 *The pre-tectonic Eğrigöz pluton* (Fig. 13g,j) - This natural example regards a N-S elongated (40x15
624 km) granite body (20.5±1.1-18.9±1.2 Ma.; Catlos et al., 2012), situated in the northern Menderes
625 metamorphic core complex and covering an area of 330 Km^2. Its geometrical features show a high
626 aspect ratio of L/W= 2.6 and an axis trend of α = 46° (parallel to the extension direction), analogous
627 to the observations made for the higher contour levels of the strongly deformed pre-tectonic Model
628 B1 (r = 1.9; θ = 42°; Fig.11d; Table 3). The 20km-long, NE-striking Gerni shear zone is closely linked

to the pulses of magmatic activity and assumed to have propagated immediately following the emplacement of the Eğrigöz pluton. Stress tensor results of the Eğrigöz pluton indicate that the shear zone has been predominant under NE-SW-trending extension. The presence of the aplitic and pegmatitic dikes along the periphery and structurally upper parts of the pluton (Erkül et al., 2017) are rather common and similarly reproduced during the analogue Model B1 experiment (Fig. 11a-b). In addition to this example, more plutons are registered carrying similar diagnostic features of pre-tectonic emplacement mode : 1) *The Totoltepec Pluton* (Kirsch et al., 2013); 2) *The Devonian granitoid of Pampa de Achala,* in Central Argentina (Simpson et al., 2001); 3) *The Koyunoba pluton* (Erkül et al., 2017).

The syn-tectonic Monzoni Intrusive Complex (Fig. 11) – This 4 km-long intrusion situated in the central Dolomites in Italy offers a great occasion for comparison due to its excellent three-dimensional exposure. However and mainly due to contact metamorphism around the pluton and the syn-metamorphic thermally driven fluid circulation, field observations are very limited, and still there is very poor knowledge of kinematic indications. Based on analogue modelling observations, new insights on the shear zone and fault structures, of the missing upper crustal layer that once hosted the emplaced magmatic chamber, is achieved. It is assumed that the pluton's emplacement mode is controlled by the Middle Triassic tectonics, however the time of emplacement (syn-tectonic or indirect post-tectonic emplacement) along the left-lateral shear zone is still under discussion. According to our model observations, this pluton exhibits diagnostic characteristics similar to a syn- to late tectonic intrusion. The pluton's long axis trends with an angle of $\alpha = -14°$, parallel to the compressional field, and shows an aspect ratio of L/W = 2 (Fig. 13k). The shape analysis of this pluton shows similarity to the Model B2 ($-10 < \theta < -19°$; r = 1.7; Fig. 11g-h). The syn-magmatic dike swarms, cropping out at the intrusion area, appear to cut the deformed sedimentary country rocks and intrude the magmatic edifice (Sloman 1989; Bonadiman et al., 1994; Gianolla et al., 2010; Abbas et al., 2018) while the pluton carries a NE–SW striking apophysis that trails the intrusion at its SW boundary. Similar natural examples of syn-tectonic emplacement mode are: 1) *The Mortagne pluton* (Román-Berdiel et al., 1997); 2) *The Los Pedroches pluton* (Aranguren et al., 1997; Román-Berdiel

et al., 2000); 3) *The Jihlava Intrusion* (Verner et al., 2006); 4) *The Hombreiro pluton* (Román-Berdiel et al., 2000); 5) *The Gulf of Aden Ridge* (Corti et al., 2003).

The post-tectonic La Tojiza Pluton (Fig. 13i,l) - The La Tojiza granite is cropping out in the Mondon˜edo Nappe Domain (Fig. 13c) and according to geochronological data it consists with a U–Pb age of 295 ± 2 Ma (Fernàndez-Suàrez et al., 2000). This post-tectonic association is composed of granite–granodiorite–tonalite–monzogranite intrusions. The intrusion reactivated the inherited transtensional tectonic structures, leading to the emplacement and formation of a sub-circular pluton of 16 km-diameter (Aranguren et al., 2003). Its thickness is estimated of 1 km and the root zone is located at its eastern border. The pluton shows an axis trend of a = -6° and parallel to the compressional field, with the pluton's aspect ratio L/W = 1.2 (Fig. 13l). Most of the observed aplitic dikes are present on the roof of the pluton and oblique to the magnetic lineation. These features are in great accordance to the lower contour levels of the post-tectonic Model B3 (θ = 0°; r = 1.4; Fig. 11k-l). The *Plasenzuela Intrusion* (Central Extremadura, Spain; Fernandez and Castro, 1999) represents another natural example for this emplacement scenario, characterised by a well-defined rounded pluton shape of low aspect ratio (L/W ~ 1).

4 Conclusions

This study provides new insights on the application of the finite pluton shape as a diagnostic indicator for constraining the tectonic setting and the relative timing of magma emplacement versus tectonics. Three scenarios on pluton emplacement (pre-, syn- and post-tectonic) in two different tectonic settings (simple shear, transtension) are tested and analysed. The intrusion shapes (aspect ratio, principal axis trend, amplitude) and the model surface deformation are measured and described, providing useful insights for the understanding of the interactions occurring between tectonics and magmatism. The main insights and conclusions supported by this study are the following:

1. Incremental strain analysis and final surface deformation reveal a different deformational pattern among the scenarios and strong interactions between tectonics and magma

emplacement. Pre-tectonic models accumulate regional strain during shearing, resulting in the delay and diffusion of the brittle structures during their up-ward propagation. Here, the final shear zone appears wider than the respective reference model and crosscut but more than one well-defined fault. Syn-tectonic emplacement causes the major boundary faults to extend and curve towards the centre and the formation of a narrow fault-controlled pull-apart basin overprinted by the master fault. The inverse shear sense, captured in strain maps, caused during intrusion is observed exclusively in the post-tectonic scenario.

2. The final shape of the intrusions emplaced along the shear zones with a different timing respect to the tectonic activity show significant deformational variations, delineating its reliability as a diagnostic feature. Observations coming from both tectonic groups (simple shear and transtension) infer parallel deformational pattern and geometrical characteristics for the intrusions of similar timing of emplacement (pre-, syn- or post-tectonic). Based on the analytical shape analysis, the asymmetric and deformed final intrusions reflect the regional stresses and finite strain field. The axis aspect ratio and trend are evolving against the contour level for each model, remaining consistent among those emplaced coevally.

3. Among the emplacement scenarios, the pre-tectonic intrusions appear strongly elongated parallel to the extension field with the lowest amplitude and the highest aspect ratios. The intrusion's flat top is cross cut by more post-emplacement shears. Syn-tectonic models are characterised by high amplitude and moderate aspect ratios. They bear acute roofs, oriented parallel to the compression direction, and scissor-tail apophysis that trails the intrusion. The sub-circular post-tectonic models show the lowest aspect ratios and a similar orientation to syn-tectonic models.

4. Faults that crosscut the central zone overprint the emplaced or up-lifting intrusion, navigating the intrusions' margins and serving as pathway for diking. The higher levels of the syn- and post-tectonic intrusion boundaries appear parallel to and constrained by the synthetic faults developing on the surface. The lateral expansion of pre-tectonic models is

bounded by the major fault structures developing subparallel to the boundary of the shear zone, while their top is overprinted by roof-diking guided by crosscutting shears.

5. The obtained diagnostic attributes are tested successfully against natural prototypes, confirming the diagnostic potential and reliability of the intrusion's shape for constraining the time and the tectonic setting of the magmatic emplacement.

Data Availability

Supplementary data to this article can be found online at: *https://dataservices.gfz-potsdam.de/xxx*

5 Acknowledgments

The experiments were performed at the HelTec - Helmholtz Laboratory for Tectonic Modelling of the Helmholtz Centre Potsdam - German Research Centre for Geosciences (GFZ), in Potsdam (Germany). The authors wish to thank F. Neumann and T. Ziegenhagen (GFZ German Research Centre for Geosciences) for their technical support and engineering. T. Román-Berdiel for her valuable reviews on a previous version of the manuscript, as well as E. Carminati (*Sapienza University)*, M. Mattei (*Roma Tre University*) and C. Bonadiman (University of Ferrara) for their constructive discussions and contributions. Part of this research was funded by the IUSS-PhD mobility grant (University of Ferrara). The research has been supported by the Deutsche Forschungsgemeinschaft (DFG) through CRC1114 "Scaling Cascades in Complex Systems", Project B01 and EPOS – the European Plate Observing System.

6 References

Abbas, H., Michail, M., Cifelli, F., Mattei, M., Gianolla, P., Lustrino, M., Carminati, E., 2018. Emplacement modes of the Ladinian plutonic rocks of the Dolomites: Insights from anisotropy of magnetic susceptibility. J. Struct. Geol. 113, 42-61. https://doi:10.1016/j.jsg.2018.05.012.

Adam, J., Urai, J.L., Wieneke, B., Oncken, O., Pfeiffer, K., Kukowski, N., Lohrmann, J., Hoth, S., Van der Zee, W., Schmatz, J., 2005. Shear localisation and strain distribution during tectonic faulting - new insights from granular-flow experiments and high-resolution optical image correlation techniques. J. Struct. Geol. 27, 283-301. https://doi:10.1016/j.jsg.2004.08.008.

Aranguren, A., Cuevas, J., Tubia, J.M., Román-Berdiel, T., Casas-Sainz, A., Casas-Ponsati, A., 2003. Granite laccolith emplacement in the Iberian arc: AMS and gravity study of the La Tojiza pluton (NW Spain). J. Geol. Soc. London. 160, 435–445. https://doi:10.1144/0016-764902-079

Bartlett, W.L., Friedman, M., Logan, J.M., 1981. Experimental folding and faulting of rocks under confining pressure Part IX. Wrench faults in limestone layers. Tectonophysics 79, 255–277. https://doi:10.1016/0040-1951(81)90116-5.

Benn, K., Odonne, F., De Saint Blanquat, M., 1998. Pluton emplacement during transpression in brittle crust: New views from analogue experiments. Geology 26, 1079–1082. https://doi:10.1130/0091-7613(1998)026<1079: PEDTIB>2.3.CO.

Benn, K., Odonne, F., Lee, S.K.Y., Darcovich, K., 2000. Analogue scale models of pluton emplacement during transpression in brittle and ductile crust. Trans. R. Soc. Edinb. Earth Sci. 91, 111–121. https://doi:10.1130/0-8137-2350-7.111.

Bonadiman, C., Coltorti, M., Siena, F., 1994. Petrogenesis and T-fO 2 estimates of Mt. Monzoni Complex (central Dolomites, Southern Alps); a Triassic shoshonitic intrusion in a transcurrent geodynamic setting. Eur. J. Mineral. 6, 943–966.

750 Brown, M., 2013. Granite: From genesis to emplacement. Geol. Soc. Am. Bull. 125, 1079–1113.
751 https://doi:10.1130/B30877.1.

752 Burov, E., Jaupart, C., and Guillou-Frottier, L., 2003. Ascent and emplacement of buoyant magma
753 bodies in brittle-ductile upper crust. J. Geophys. Res. 108. https://doi: 10.1029/2002JB001904

754 Catlos, E. J., Jacob, L., Oyman, T., & Sorensen, S., 2012. Long-term exhumation of an Aegean
755 metamorphic core complex granitoids in the Northern Menderes Massif, western Turkey. Amer-
756 ican Journal of Science, 312(5), 534-571.

757 Castro, A., Fernández, C., 1998. Granite intrusion by externally induced growth and deformation of
758 the magma reservoir, the example of the Plasenzuela pluton, Spain. J. Struct. Geol. 20, 1219–
759 1228. https://doi:10.1016/S0191-8141(98)00056-X.

760 Corti, G., Bonini, M., Conticelli, S., Innocenti, F., Manetti, P., Sokoutis, D., 2003. Analogue modelling
761 of continental extension: A review focused on the relations between the patterns of deformation
762 and the presence of magma. Earth-Science Rev. 63, 169–247. https://doi:10.1016/S0012-
763 8252(03)00035-7.

764 Corti, G., Moratti, G., Sani, F., 2005. Relations between surface faulting and granite intrusions in
765 analogue models of strike-slip deformation. J. Struct. Geol. 27, 1547–1562.
766 https://doi:10.1016/j.jsg.2005.05.011.

767 De Saint Blanquat, M., Horsman, E., Habert, G., Morgan, S., Vanderhaeghe, O., Law, R., Tikoff, B.,
768 2011. Multiscale magmatic cyclicity, duration of pluton construction, and the paradoxical rela-
769 tionship between tectonism and plutonism in continental arcs. Tectonophysics 500, 20–33.
770 https://doi:10.1016/j.tecto.2009.12.009.

771 Dooley, T.P., Schreurs, G., 2012. Analogue modelling of intraplate strike-slip tectonics: A review
772 and new experimental results. Tectonophysics 790, 574-575, 1–71.
773 https://doi.org/10.1016/j.tecto.2012.05.030.

774 Erkül F., Erkül, S.T., Manap, H.S., Çolak, C., 2017. An extensional and transtensional origin of elon-
775 gated magmatic domes and localised transfer faults in the northern Menderes metamorphic
776 core complex, western Turkey. Geodinamica Acta 29, 139-159.
777 https://doi:10.1080/09853111.2017.1343523.

778 Ennih, N., Liégeois, J.P., 2001. The Moroccan Anti-Atlas: The West African craton passive margin
779 with limited Pan-African activity. Implications for the northern limit of the craton. Precambrian
780 Res. 112, 289–302. https://doi:10.1016/S0301-9268(01)00195-4.

781 Fernández, C., Castro, A., 1999. Pluton accommodation at high strain rates in the upper continental
782 crust. The example of the Central Extremadura batholith, Spain. J. Struct. Geol. 21, 1143–1149.
783 https://doi:10.1016/S0191-8141(99)00086-3.

784 Fernández, C., Castro, A., 1999. Pluton accommodation at high strain rates in the upper continental
785 crust. The example of the Central Extremadura batholith, Spain. J. Struct. Geol. 21, 1143–1149.
786 https://doi:10.1016/S0191-8141(99)00086-3.

787 Fernández-Suárez, J., Dunning, G.R., Jenner, G.A., and Gutiérrez-Alonso, G., (2000). Variscan col-
788 lisional magmatism and deformation in NW Iberia: constraints from U-Pb geochronology of
789 granitoids. J. Geol. Soc. 157, 565-576.

790 Ferré, E.C., Galland, O., Montanari, D., Kalakay, T.J., 2012. Granite magma migration and emplace-
791 ment along thrusts. Int. J. Earth Sci. 101, 1673–1688. https://doi:10.1007/s00531-012-0747-6.

792 Fossen, H., Teyssier, C., Whitney, D.L., 2013. Transtensional folding. J. Struct. Geol. 56, 89–102.
793 https://doi:10.1016/j.jsg.2013.09.004.

794 Galland, O., Holohan, E., van Wyk de Vries, B., Burchardt, S., 2015. Laboratory Modelling of Vol-
795 cano Plumbing Systems: A Review. In: Breitkreuz C., Rocchi S. (eds) Physical Geology of Shal-
796 low Magmatic Systems. Adv. Volcanol. Springer, 1-68. https://doi:10.1007/11157_2015_9.

797 Galland, O., Cobbold, P.R., de Bremond d'Ars, J., Hallot, E., 2007b. Rise and emplacement of
798 magma during horizontal shortening of the brittle crust: Insights from experimental modeling. J.
799 Geophys. Res. Solid Earth 112, 1–21. https://doi:10.1029/2006JB004604.

800 Galland, O., Cobbold, P.R., Hallot, E., de Bremond d'Ars, J., Delavaud, G., 2006. Use of vegetable
801 oil and silica powder for scale modelling of magmatic intrusion in a deforming brittle crust. Earth
802 Planet. Sci. Lett. 243, 786–804. https://doi:10.1016/j.epsl.2006.01.014.

803 Galland, O., de Bremond d'Ars, J., Cobbold, P.R., Hallot, E., 2003. Physical models of magmatic
804 intrusion during thrusting. Terra Nova 15, 405–409. https://doi:10.1046/j.1365-
805 3121.2003.00512.x.

806 Galland, O., Hallot, E., Cobbold, P.R., Ruffet, G., de Bremond d'Ars, J., 2007a. Volcanism in a
807 compressional Andean setting: A structural and geochronological study of Tromen volcano
808 (Neuquén province, Argentina). Tectonics 26. https://doi:10.1029/2006TC002011.

809 Gasquet, D., Ennih, N., Liegeois, J.P., Soulaimani, A., Michard, A., 2008. The Pan-African Belt, in:
810 Continental Evolution: The Geology of Morocco. Lecture Notes in Earth Sciences. 33–64.

811 Gomes, A.S., Rosas F.M., Duarte J.C., Schellart W.P., Almeida J., Tomás, R., Strak, V., 2019. An-
812 alogue modelling of the brittle shear zone propagation across upper crustal morpho-rheological
813 heterogeneities. J. Struct. Geol. 126, 175-197. https://doi: 10.1016/j.jsg.2019.06.004.

814 Handy, M.R., Mulch, A., Rosenau, M. and Rosenberg, C. L., 2001. The role of fault zones and melts
815 as agents of weakening, hardening and differentiation of the continental crust: a synthesis.
816 Geol. Soc. Spec. Publ., 186, 305–332. https://doi:10.1144/GSL.SP.2001.186.01.18.

817 Handy, M.R., Streit, J.E., 1999. Mechanics and mechanisms of magmatic underplating: Inferences
818 from mafic veins in deep crustal mylonite. Earth Planet. Sci. Lett. 165, 271–286.
819 https://doi:10.1016/S0012-821X(98)00272-6.

820 Holohan, E.P., Van Wyk de Vries, B., Troll, V.R., 2008. Analogue models of caldera collapse in
821 strike-slip tectonic regimes. Bull. Volcanol.70, 773–796. https://doi .org /10 .1007 /s00445 -007
822 -0166 -x. Hubbert, M.K., 1937. Theory of scalable models as applied to the study of geologic
823 structures. Geol. Soc. Am. Bull. 48, 1459–1520. doi:10.1130/GSAB-48-1459.

824 Hutton, D.H.W., Reavy, R.J., 1992. Strike-slip tectonics and granite petrogenesis. Tectonics 11,
825 960–967. https://doi:10.1029/92TC00336.

826 Hutton, D.H.W., 1988. Granite emplacement mechanisms and tectonic controls: inferences from
827 deformation studies. Trans. R. Soc. Edinb. Earth Sci. 79, 245–255.
828 https://doi:10.1017/S0263593300014255.

829 Kirsch, M., Keppie, J.D., Murphy, J.B., Lee, J.K.W., 2013. Arc plutonism in a transtensional regime:
830 The late Palaeozoic Totoltepec pluton, Acatlán Complex, southern Mexico. Int. Geol. Rev. 55,
831 263–286. https://doi:10.1080/00206814.2012.693247.

832 Klinkmüller, M., Schreurs, G., Rosenau, M., Kemnitz, H., 2016. Properties of granular analogue
833 model materials: A community wide survey. Tectonophysics 684, 23–38.
834 https://doi:10.1016/j.tecto.2016.01.017.

835 Koptev, A., Burov, E., Gerya, T., Le Pourhiet, L., Leroy, S., Calais, E., Jolivet, L., 2017. Plume-
836 induced continental rifting and break-up in ultra-slow extension context: Insights from 3D nu-
837 merical modeling. Tectonophysics. Article in press. https://doi:10.1016/j.tecto.2017.03.025.

838 Verner, K., Žák J., Hrouda, F., Holub, F., 2006. Magma emplacement during exhumation of the
839 lower- to mid-crustal orogenic root: the Jihlava syenitoid pluton, Moldanubian Unit, Bohemian
840 Massif. J Struct Geol. 28,1553–1567.

841 Mandal, N., Chakraborty, C., 1990. Strain fields and foliation trajectories around pre-, syn-, and post-
842 tectonic plutons in coaxially deformed terranes. Geol. J. 25, 19–33.
843 https://doi:10.1002/gj.3350250103.

844 Mazzarini, F., Musumeci, G., Montanari, D., Corti, G., 2010. Relations between deformation and
845 upper crustal magma emplacement in laboratory physical models. Tectonophysics 484, 139–
846 146. https://doi:10.1016/j.tecto.2009.09.013.

847 Michail, M., Rudolf, M., Rosenau, M., Riva A., Gianolla, P., Coltorti, M., 2020. Digital image correla-
848 tion data from analogue modelling experiments addressing magma emplacement along simple
849 shear and transtensional fault zones. GFZ Data Services.
850 http://doi.org/10.5880/fidgeo2020.033.

851 Montanari, D., Corti, G., Sani, F., Del Ventisette, C., Bonini, M., Moratti, G., 2010. Experimental
852 investigation on granite emplacement during shortening. Tectonophysics 484, 147–155.
853 https://doi:10.1016/j.tecto.2009.09.010.

854 Paterson, S.R., Okaya, D., Memeti, V., Economos, R., Miller, R.B., 2011. Magma addition and flux
855 calculations of incrementally constructed magma chambers in continental margin arcs: Com-
856 bined field, geochronologic, and thermal modeling studies. Geosphere 7, 1439–1468.
857 https://doi:10.1130/GES00696.1.

858 Paterson, S.R., Schmidt, K.L., 1999. Is there a close relationship between faults and plutons? J.
859 Struct. Geol. 21, 1131–1142.

860 Paterson, S.R., Tobisch, O.T., 1988. Using pluton ages to date regional deformations: problems
861 with commonly used criteria. Geology 16, 1108–1111.

862 Petford, N., Cruden, A.R., McCaffrey, K.J., Vigneresse, J.-L., 2000. Granite magma formation,
863 transport and emplacement in the Earth's crust. Nature 408, 669–673.
864 https://doi:10.1038/35047000.

865 Ramberg, H., 1981. Gravity, deformation and the Earth's crust: In Theory, Experiments, and Geo-
866 logical Application. London, Academic Press, 452.

867 Ribe, N.M., Davaille, A., 2013. Dynamical similarity and density (non-) proportionality in experi-
868 mental tectonics. Tectonophysics608, 1371-1379. https://doi:10.1016/j.tecto.2013.06.005.

869 Riedel, W., 1929. Zur Mechanik geologischer Brucherscheinungen. Zentralblatt Mineral., Geol. u.
870 Paläont. B, 354–368.

871 Ritter, M.C., Leever, K., Rosenau, M., Oncken, O., 2016. Scaling the sandbox-Mechanical (dis)
872 similarities of granular materials and brittle rock. Journal of Geophysical Research: Solid Earth,
873 121(9), 6863–6879. https://doi:10.1002/2016jb012915.

874 Román-Berdiel, T., 1999. Geometry of granite emplacement in the upper crust: contributions of
875 analogue modelling, in: Castro, A., Fernandez, C., Vigneresse, J.L. (Eds.), Understanding
876 granites: Integrating new and classical techniques. Geological Society, London, Special Publi-
877 cations. 168. 77–94. https://doi:10.1144/GSL.SP.1999.168.01.06.
878
879 Román-Berdiel, T., Aranguren, A., Cuevas, J.L., Tubia, J.M., Gapais, D., Brun, J.-P., 2000. Experi-
880 ments on granite intrusion in transtension, in: Vendeville, B., Mart, Y., Vigneresse, J.L. (Eds.),
881 Salt, Shale and Igneous Diapirs in and around Europe. Geological Society, London, Special
882 Publications. 174. 21–42. https://doi:10.1144/GSL.SP.1999.174.01.02.

883 Román-Berdiel, T., Gapais, D., Brun, J.P., 1997. Granite intrusion along strike-slip zones in experi-
884 ment and nature. Am. J. Sci. 297, 651–678. https://doi:10.2475/ajs.297.6.651.

885 Rosenberg, C.L., 2004. Shear zones and magma ascent: A model based on a review of the Tertiary
886 magmatism in the Alps. Tectonics 23, 21. https://doi:10.1029/2003TC001526.

887 Rosenau et al. (2018): Ring-shear test data of quartz sand G12 used for analogue experiments in
888 the Helmholtz Laboratory for Tectonic Modelling (HelTec) at the GFZ German Research Centre
889 for Geosciences in Potsdam. GFZ Data Services. https://doi:10.5880/GFZ.4.1.2019.003.

890 Rudolf, M., Boutelier, D., Rosenau, M., Schreurs, G., Oncken, O., 2016. Rheological benchmark of
891 silicone oils used for analog modeling of short- and long-term lithospheric deformation. Tecto-
892 nophysics 684, 12–22. https://doi:10.1016/j.tecto.2015.11.028.

893 Sant'Ovaia, H., Bouchez, J.L., Noronha, F., Leblanc, D., Vigneresse, J.L., 2000. Composite-laccolith
894 emplacement of the post-tectonic Vila Pouca de Aguiar granite pluton (northern Portugal): A
895 combined AMS and gravity study. Trans. R. Soc. Edinb. Earth Sci. 91, 123–137.
896 https://doi:10.1017/S026359330000732X.

897 Schellart, W.P., Strak, V., 2016. A review of analogue modelling of geodynamic processes: Ap-
898 proaches, scaling, materials and quantification, with an application to subduction experiments.
899 J. Geodyn. 100, 7-32. https://doi:10.1016/j.jog.2016.03.009.

900 Schöpfer, M.P.J., Steyrer, H.P., 2001. Experimental modeling of strike-slip faults and the self-similar
901 behavior. Geol. Soc. Am. Mem. 193, 21–27. https://doi:10.1130/0-8137-1193-2.21.

902 Schreurs, G., 2003. Fault development and interaction in distributed strike-slip shear zones: an ex-
903 perimental approach, in: Storti, F., Holdsworth, R.E., Salvini, F. (Eds.), Intraplate Strike-Slip
904 deformation belts. Geological Society, London, Special Publications. 35–52.
905 https://doi:10.1144/GSL.SP.2003.210.01.03.

906 Shinevar, W.J., Behn, M.D., Hirth, G., 2015. Compositional dependence lower crustal viscosity, Ge-
907 ophys. Res. Lett. 42, 8333–8340. https://doi:10.1002/2015GL065459.

908 Simpson, C., Whitmeyer, S.J., De Paor, D., Gromet, L.P., Miro, R., Krol, M., and Short, H., 2001.
909 Sequential ductile to brittle reactivation of major fault zones along the accretionary margin of
910 Gondwana in Central Argentina. In: Holdsworth, R.E. et al. (eds.) The Nature and Tectonic
911 Significance of Fault Zone Weakening. Geol. Soc. London, Special Publications, 186, 233-255.

912 Sloman, L., 1989. Triassic shoshonites from the Dolomites, northern Italy: alkaline arc rocks in a
913 strike-slip setting. J. Geophys. Res. 94, 4655–4666.

914 Vigneresse, J.L., 1995. Control of granite emplacement by regional deformation. Tectonophysics
915 249, 173–186. https://doi:10.1016/0040-1951(95)00004-7.

916 Vigneresse, J.L., Bouchez, J.L., 1997. Successive Granitic Magma Batches During Pluton Emplace-
917 ment: the Case of Cabeza de Araya (Spain). J. Petrol. 38, 1767–1776.
918 https://doi.org/10.1093/petroj/38.12.1767.

919 Visonà, D., Zanferrari, A., 2002. Some constraints on geochemical features in the Triassic mantle
920 of the easternmost Austroalpine-Southalpine domain: evidence from the Karawanken pluton
921 (Carinthia, Austria). International Journal of Earth Sciences, 89 (2000), 40-51.

922 Weijermars, R., Schmeling, H., 1986. Scaling of Newtonian and non-Newtonian fluid dynamics with-
923 out inertia for quantitative modelling of rock flow due to gravity (including the concept of rheo-
924 logical similarity). Phys. Earth Planet. Inter. 43, 316–330. https://doi:10.1016/0031-
925 9201(86)90021-X.

926 Westoby, M.J., Brasington, J., Glasser, N.F., Hambrey, M.J. & Reynolds, J.M., 2012. Structure-
927 from-Motion photogrammetry: A low-cost, effective tool for geoscience applications. Geomor-
928 phology, 179, 300-314. doi:10.1016/j.geomorph.2012.08.021.

929 Wilcox, R.E., Harding, T.P., Seely, D.R., 1973. Basic wrench tectonics. Am. Assoc. Pet. Geol. Bull.
930 57, 74–96. https://doi:10.1306/819A424A-16C5-11D7-8645000102C1865D.

931 Xiao, Y., Wu, G., Lei, Y., Chen, T., 2017. Analogue modeling of through-going process and devel-
932 opment pattern of strike-slip fault zone. Pet. Explor. Dev. 44, 368–376.
933 https://doi:10.1016/S1876-3804(17)30043-5.

934

935 7 Tables

936 **Table 1 Model characteristics and experimental conditions**

Models	Thickness of brittle layer	Thickness of ductile layer	Intrusion rate, Ir	Injected Volume, Iv	Relative displacement rate, Dv	Total horizontal displacement, Dt	Experiment Duration
Reference models (Group R)							
Simple shear RS	40mm	7mm	-	-	1.0 mm/min	30 mm	30 min
Transtension RT	40mm	7mm	-	-	1.0 mm/min	30 mm	30 min
Static Intrusion R0	40mm	7mm	21.0 mm^3/s	$37.7x10^3mm^3$	-	-	30 min
Simple shear models (Group A)							
Pre-tectonic intrusion A1	40mm	7mm	21.0 mm^3/s	$37.7x10^3mm^3$	1.0 mm/min	30 mm	60 min
Syn-Tectonic Intrusion A2	40mm	7mm	21.0 mm^3/s	$37.7x10^3mm^3$	1.0 mm/min	30 mm	30 min
Post-tectonic intrusion A3	40mm	7mm	21.0 mm^3/s	$37.7x10^3mm^3$	1.0 mm/min	30 mm	60 min
Transtension models (Group B)							
Pre-tectonic intrusion B1	40mm	7mm	21.0 mm^3/s	$37.7x10^3mm^3$	1.0 mm/min	30 mm	60 min
Syn-Tectonic Intrusion B2	40mm	7mm	21.0 mm^3/s	$37.7x10^3mm^3$	1.0 mm/min	30 mm	30 min
Post-tectonic intrusion B3	40mm	7mm	21.0 mm^3/s	$37.7x10^3mm^3$	1.0 mm/min	30 mm	60 min

937

938 **Table 2 Material properties and scaling factors**

Parameters	Models	Nature	Model/ Nature (Scaling factor)
Brittle material	Quartz Sand	Upper Crust	
Length, L	0.01 m	0.6 - 6 km	$0.6 - 6 \times 10^{-6}$
Cohesion, C	10-100 Pa	10 MPa	$1\text{-}10 \times 10^{-6}$
Density, ρ	1600 Kg/m	2600 kg/m	0.615
Gravity, g	9.81 m/s	9.81 m/s	1
Viscous material	Silicone oil	Intrusion/ shear zone	
Viscosity, η	3×10^{4} Pa s	$>10^{18}$ Pa s	3.0×10^{-14}
Density, ρ	965 kg/m	1600 kg/m	0.603
Time, t	1 sec	30000 yrs	10^{-13}

939

940 **Table 3 Summarizing table of diagnostic attributes as suggested by the analogue models for the different em-**
941 **placement scenarios.**

Model	Pluton Elongation [a]		Orientation [a]	Dike system	Pluton Amplitude, A
	Group A	*Group B*			
Pre-tectonic	**High** (r_{A1} >1.5)	**High** (r_{B1} >1.5)	Long axis // extension	Roof	**Low**
Syn-Tectonic	**High** (r_{A2} >1.5)	**Medium/High** [b] (r_{B2} >1.5)	Long axis // compression	Lateral (apophysis)	**High**
Post-tectonic	**Low** (r_{A3} <1.5)	**Low** (r_{B3} <1.5)	Long axis // compression	Roof	**Medium**

942 [a] Based on an ellipse fitted to the lower (C_1) and higher (C_2) contour level of the intrusion.

943 [b] Based on repetition models (100, 59, 95; see Appendix A.1)

8 Figures and Captions

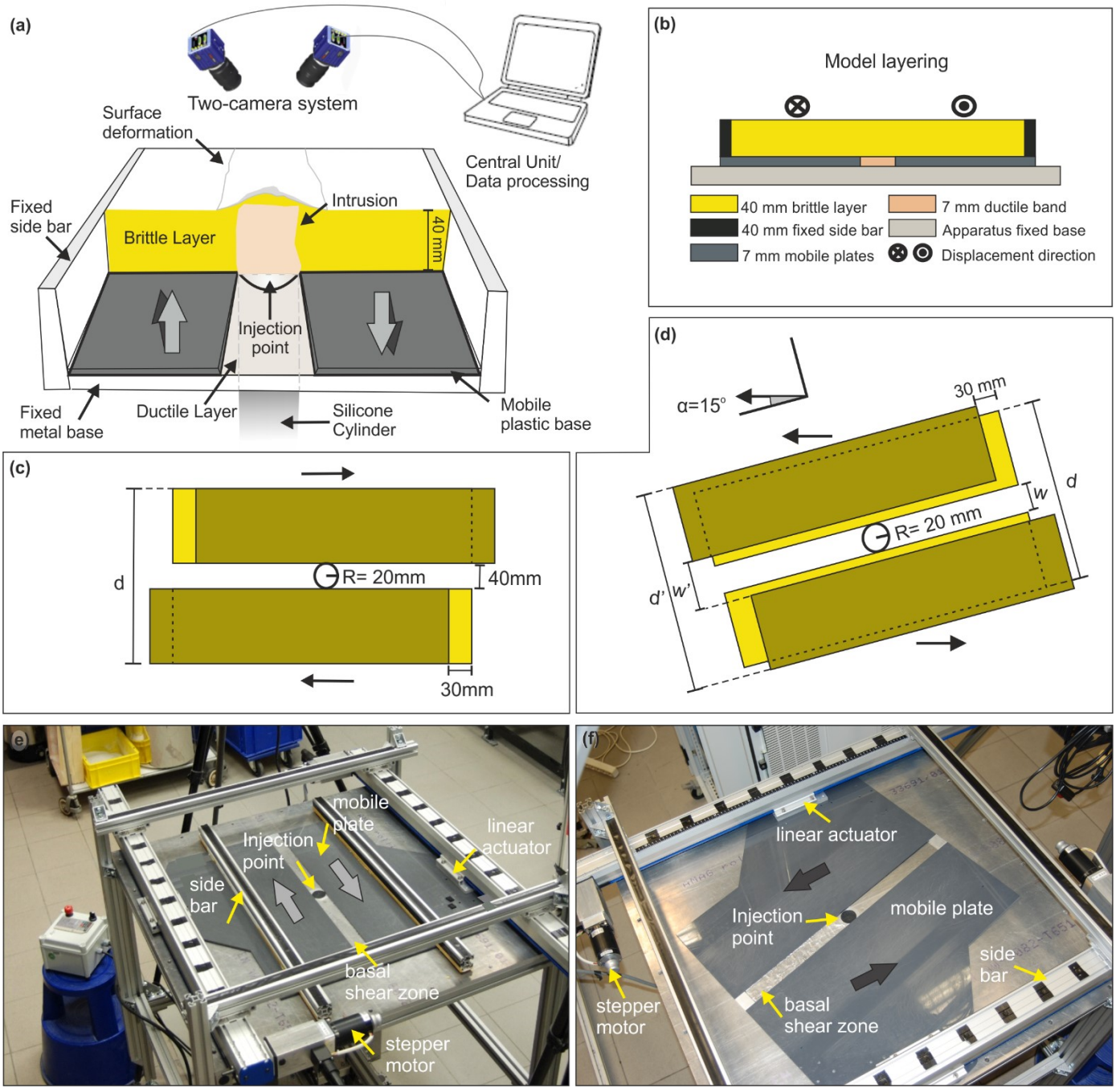

Fig. 1 Details of the experimental apparatus. Details of the experimental set-up. (a) Schematic cut-out 3D view depicting its various components; (b) Model layering; kinematic basal boundary conditions for (c) Sketch of the experimental setting of the simple shear deformation (d= 310 mm) and (d) the transtensional deformation (obliquity α=15°) with the initial (yellow) and final (green) positions of the mobile plates (w= 40 mm, w'= 55.5 mm, d= 360 mm, d'= 375.5 mm; Oblique view of experimental settings for (e) simple shear and (f) transtensional deformation. Arrows indicate the direction of plate movement.

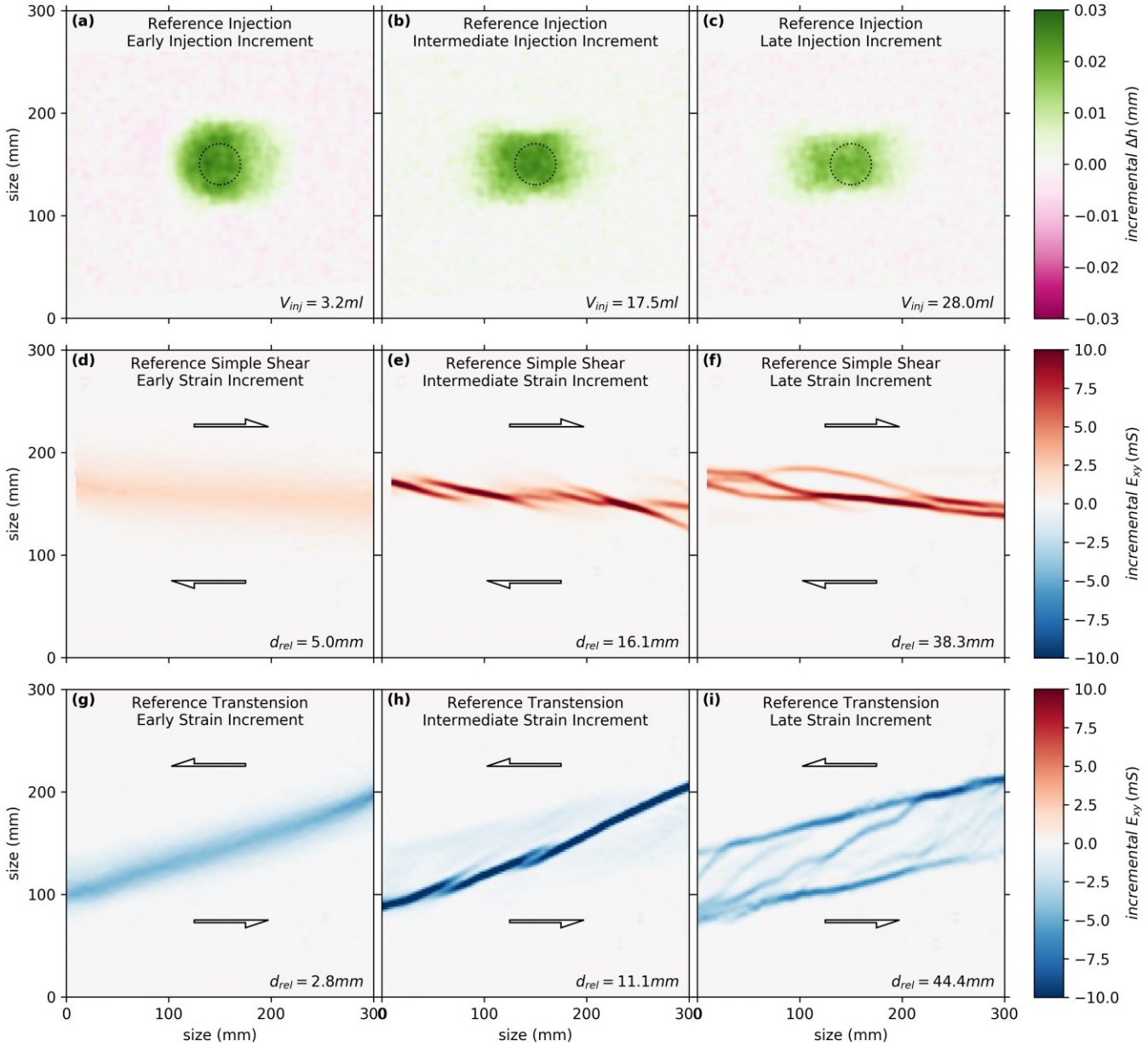

952

953 **Fig. 2 Surface evolution and deformational pattern of the reference experiments(Group R): (a-c) representative**
954 **stages (with V_{inj} = 3.2, 17.5, 28.0 ml) of the topographic evolution (vertical displacement Δh) of the static intru-**
955 **sion model R0; (d-f) representative stages (at d_{rel} = 5.0, 16.1, 38.3 mm) of the strain field (shear stain Exy) of the**
956 **simple shear model RS and (g-i) representative stages (at d_{rel} = 5.0, 16.1, 38.3 mm) of the strain field (shear stain**
957 **Exy) of the transtension model RT. Positive values of Exy (in red) indicate a dextral shear sense and negative**
958 **values (in blue) indicate sinistral shear. Dotted circles indicate the position of the basal injection.**

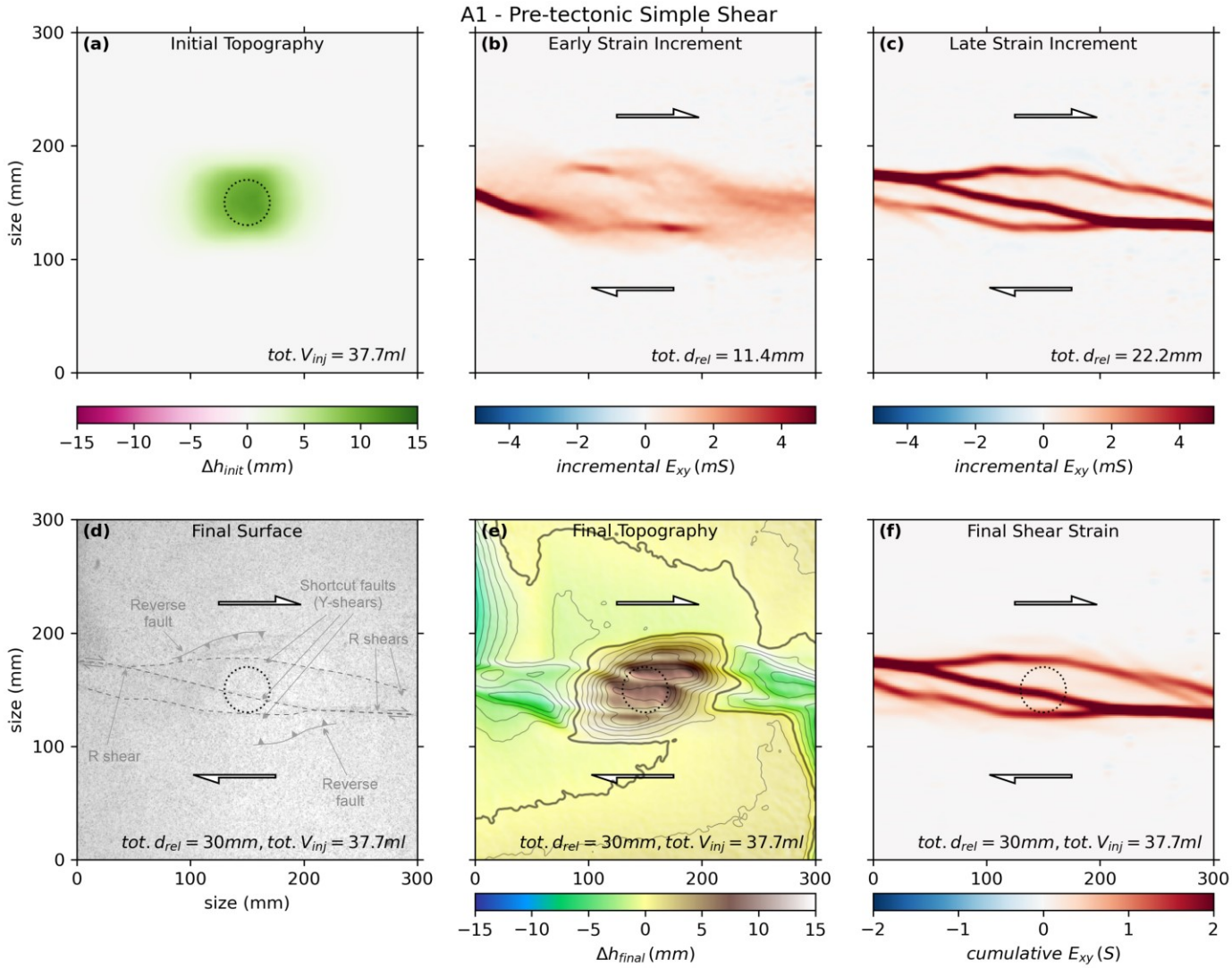

Fig. 3 Surface deformation of the pre-tectonic intrusion model in simple shear (Model A1). Shown are snapshots of the evolution: (a) Topography the end of static intrusion (V_{inj} = 37.7 ml), (b) incremental strain during an early stage of displacement (d_{rel} = 11.4 mm), and (c) during a late stage (d_{rel} = 22.2 mm). Panels in the second row show the final (cumulative deformation) stage of the model (d_{rel} = 30 mm, V_{inj} = 37.7 ml): (d) surface image; (e) cumulative vertical displacement (tot. d_{rel}=30mm) and (f) cumulative shear strain (E_{xy}). Dotted circles indicate the position of the basal injection.

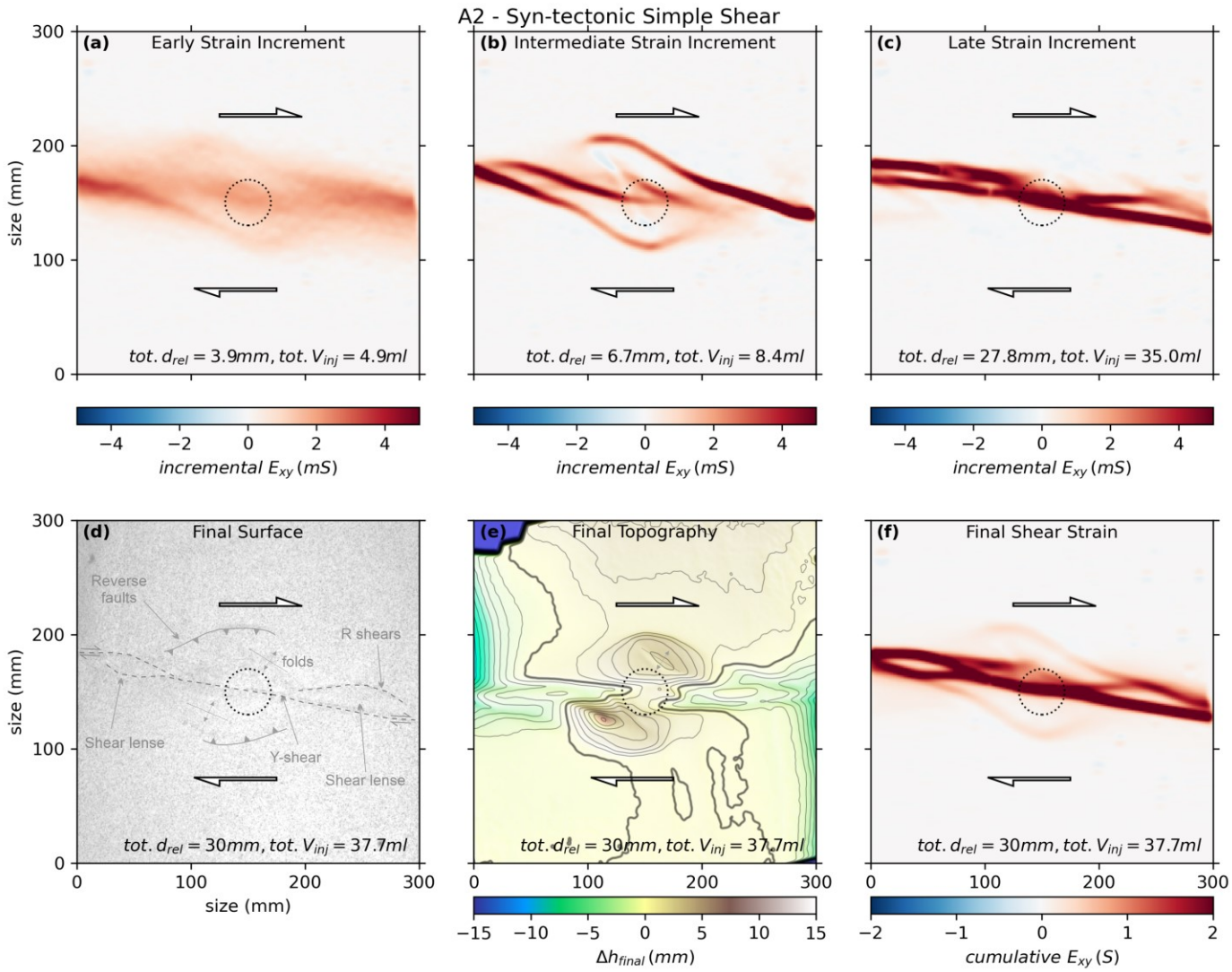

966

967 **Fig. 4 Surface deformation of the syn-tectonic intrusion model in simple shear (Model A2). Shown are snapshots**
968 **of the evolution: Incremental strain during an (a) early (V_{inj} = 4.9 ml and d_{rel} = 6.7 mm), (b) intermediate (V_{inj} = 8.4**
969 **ml and d_{rel} = 6.7 mm) and (c) late stage (V_{inj} = 35.0 ml and d_{rel} = 27.8 mm). Panels in the second row show the**
970 **final (cumulative deformation) stage (d_{rel} = 30 mm, V_{inj} = 37.7 ml): (d) surface image; (e) cumulative vertical**
971 **displacement (tot. d_{rel}=30mm) and (f) cumulative shear strain (E_{xy}). Dotted circles indicate the position of the**
972 **basal injection.**

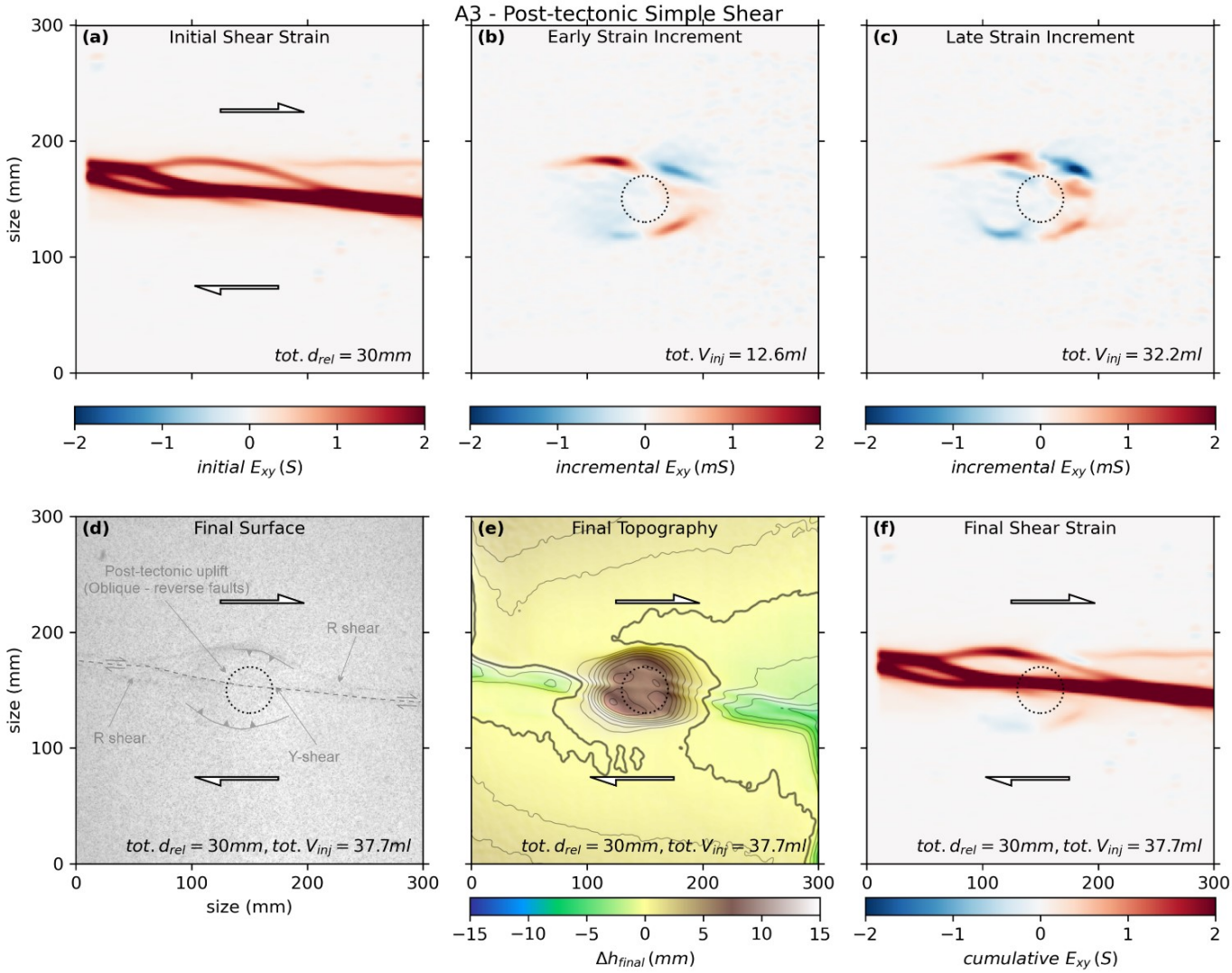

973

974 **Fig. 5 Surface deformation of the post-tectonic intrusion model in simple shear (Model A3). Shown are snap-**
975 **shots of the evolution: (a) Accumulated strain at the beginning of intrusion (d_{rel} = 30 mm), (b) incremental strain**
976 **during an early (V_{inj} = 12.6 ml) and (c) late stage (V_{inj} = 32.2 ml) of intrusion. Panels in the second row show the**
977 **final (cumulative deformation) stage (d_{rel} = 30 mm, V_{inj} = 37.7 ml): (d) surface image; (e) cumulative vertical**
978 **displacement (tot. d_{rel}=30mm) and (f) cumulative shear strain (E_{xy}). Dotted circles indicate the position of the**
979 **basal injection.**

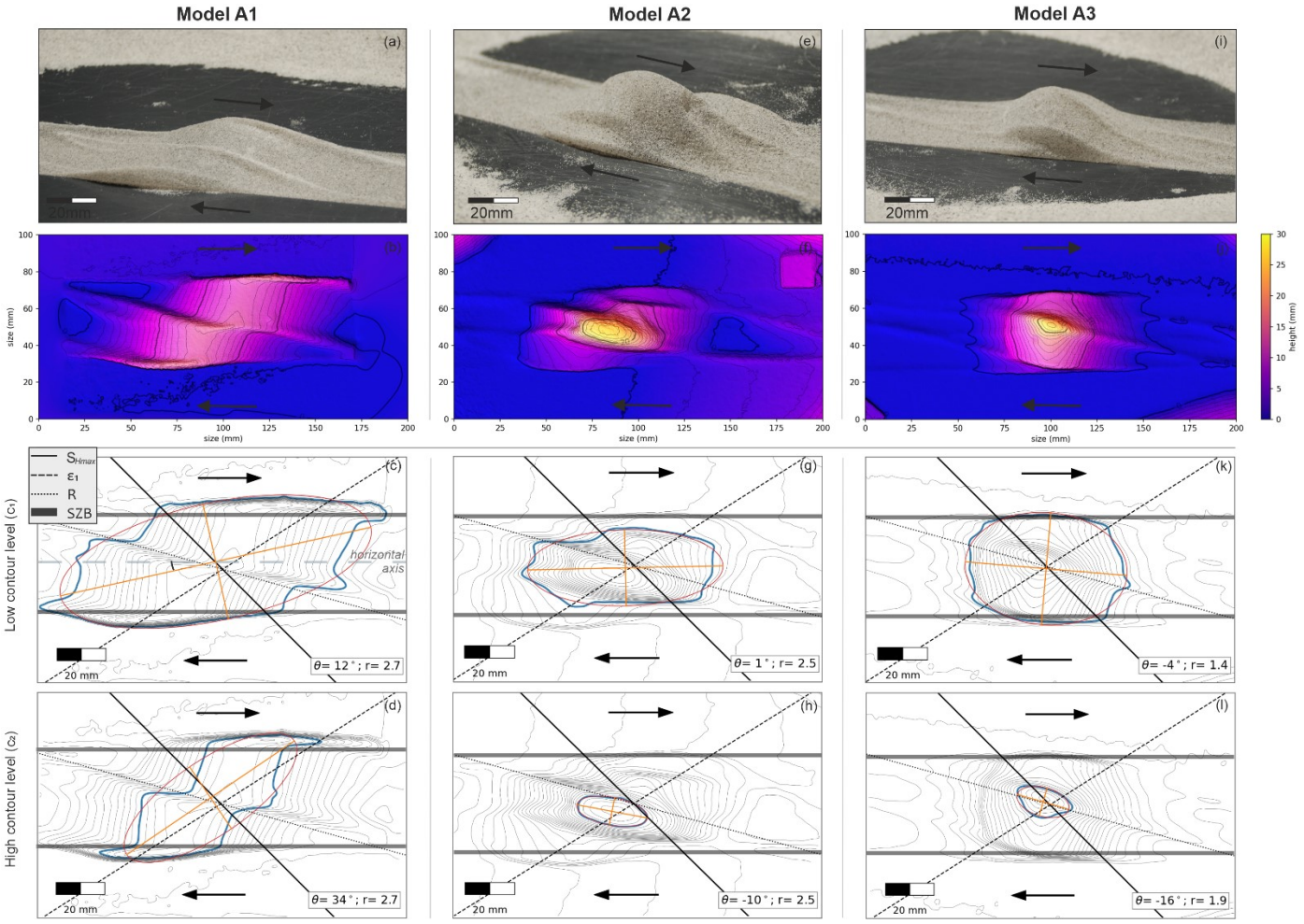

Fig. 6 Models of the intrusions in the simple shear regime (Group A): Model A1 (a-c); Model A2 (d-f) and Model A3 (g-i). (a, d, g) Oblique views of the excavated intrusions; (b, e, h) Digital Intrusion Models (DIM) coloured and with contour lines; (c, f, i) Orientation and geometry of the intrusion (in map view), where θ = the angle between the long axis (orange) of the fitted ellipse (red) and the strike of the basal shear zone. r is the intrusion's aspect ratio (length-to-width ratio, L/W). Light and dark grey quadrants indicate contraction and extensional quadrants, respectively.

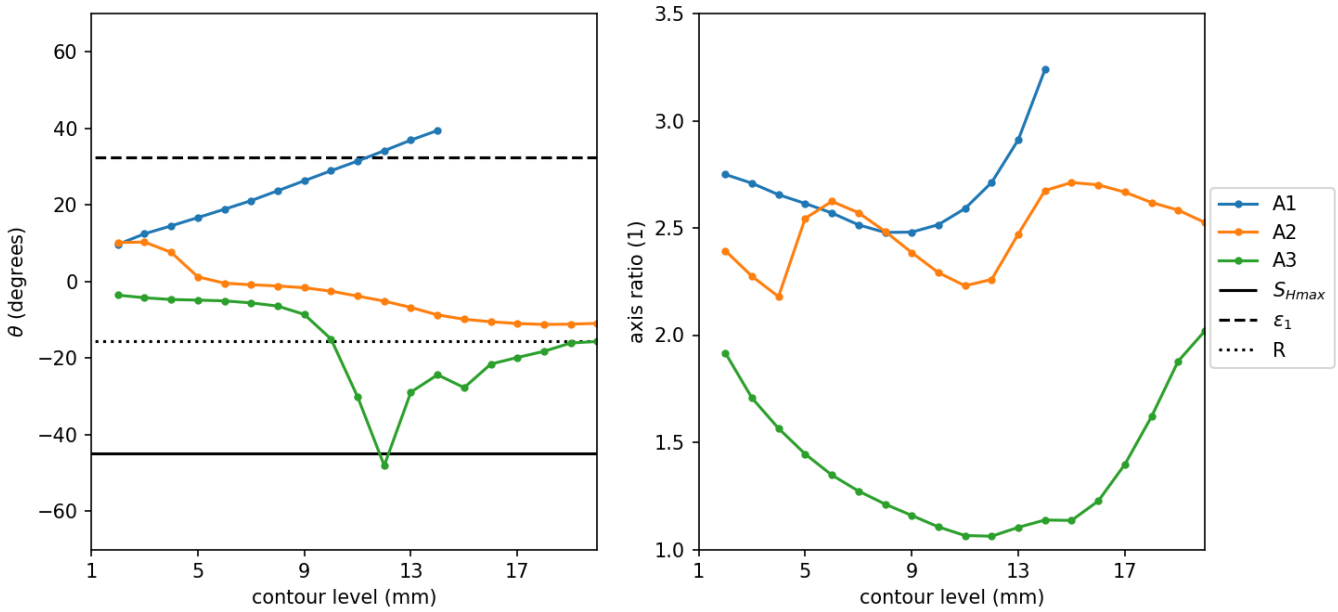

987

988 **Fig. 7 Series A experimental results expressed in graph of angles and ratios ellipses vs. intrusion contour level.**

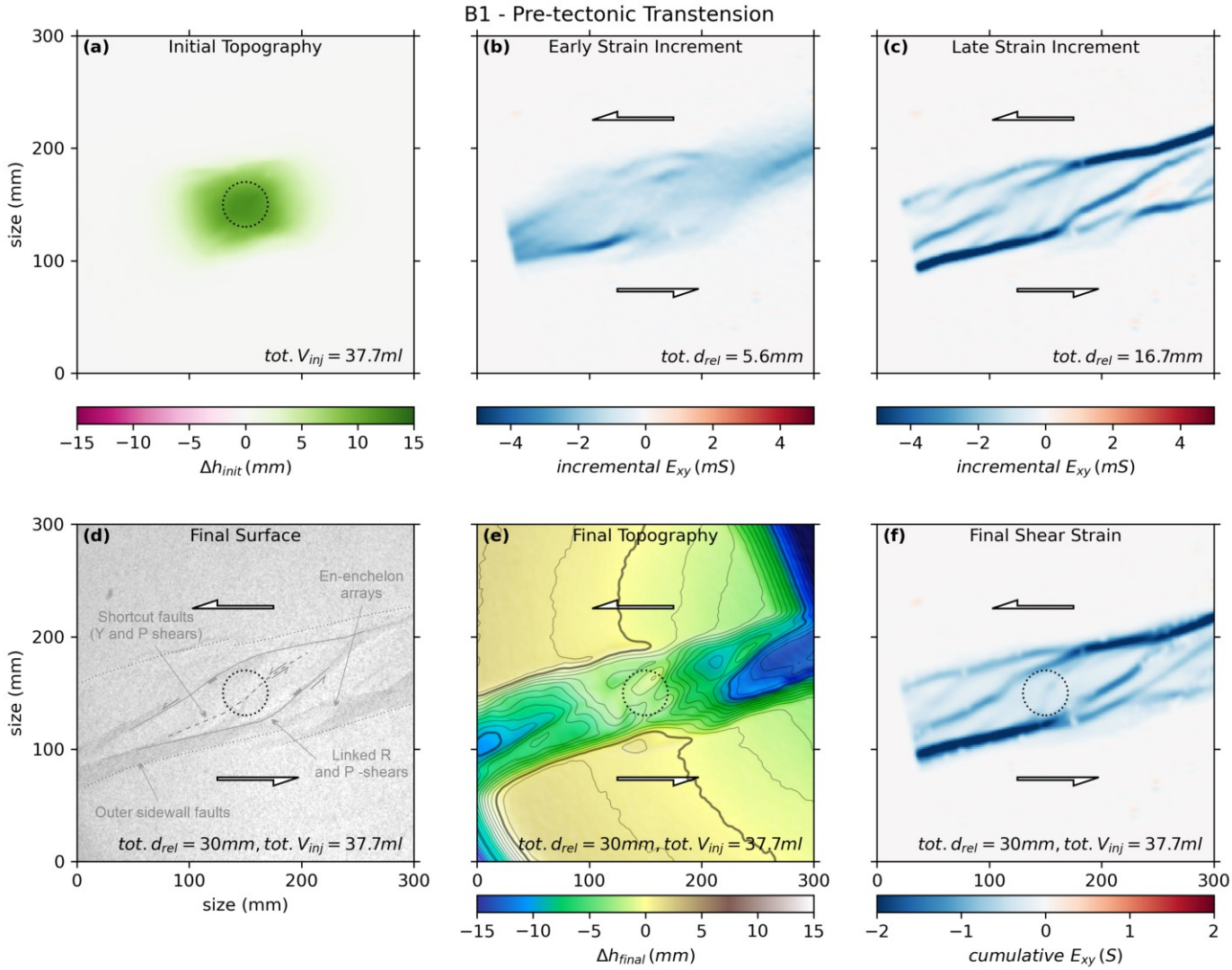

Fig. 8 Surface deformation of the pre-tectonic intrusion model in transtension (Model B1). Shown are snapshots representative of the evolution: (a) Topography the end of static intrusion (V_{inj} = 37.7 ml), (b) incremental strain during an early stage of displacement (d_{rel} = 5.6 mm), and (c) during a late stage (d_{rel} = 16.7 mm). Panels in the second row show the final (cumulative deformation) stage of the model (d_{rel} = 30 mm, V_{inj} = 37.7 ml): (d) surface image; (e) cumulative vertical displacement (tot. d_{rel}=30mm) and (f) cumulative shear strain (E_{xy}). Dotted circles indicate the position of the basal injection.

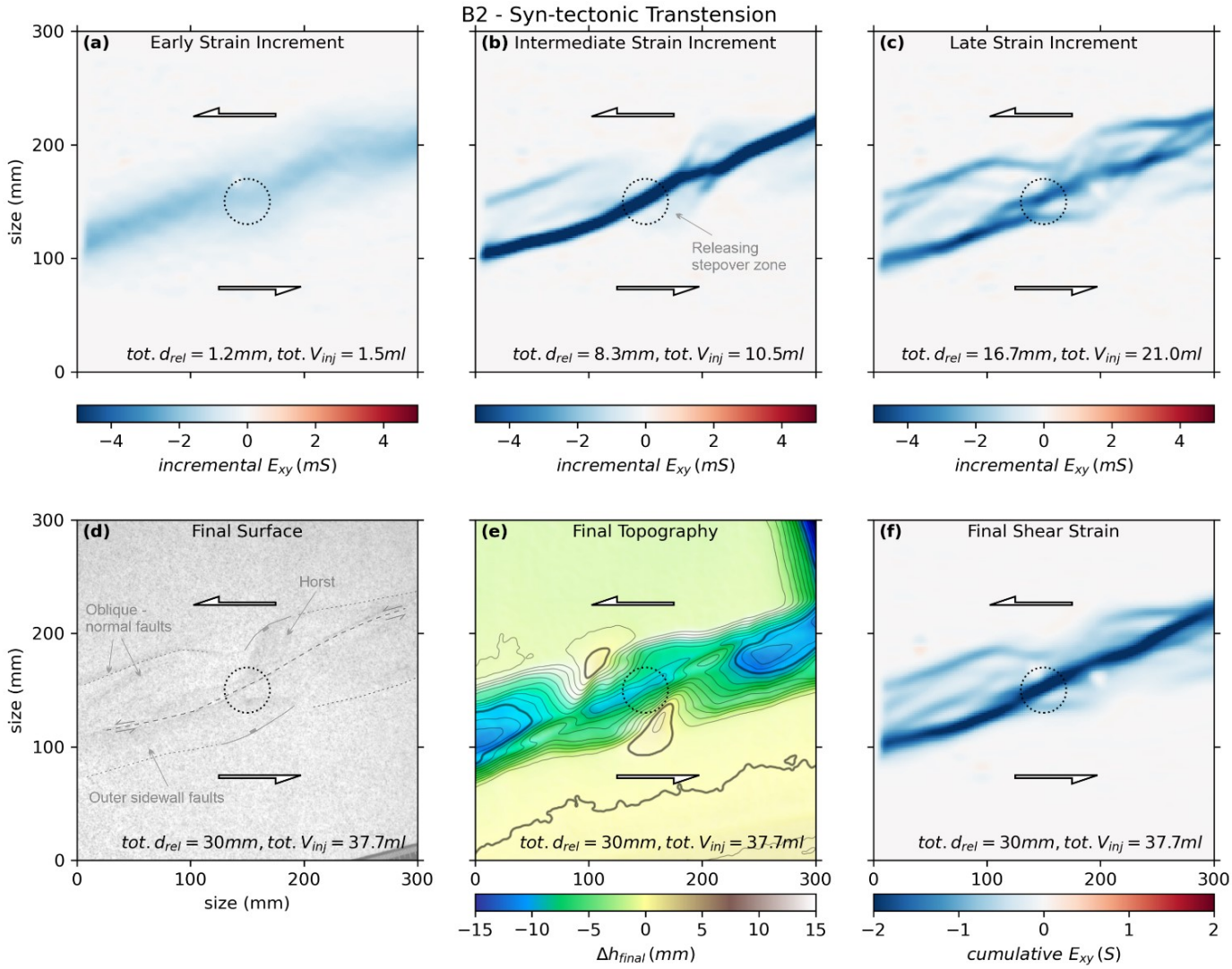

996

997 **Fig. 9 Surface deformation of the syn-tectonic intrusion model in transtension (Model B2). Shown are snapshots**
998 **representative of the evolution: Incremental strain during an (a) early (V_{inj} = 1.5 ml and d_{rel} = 1.2 mm), (b) inter-**
999 **mediate (V_{inj} = 10.5 ml and d_{rel} = 8.3 mm) and (c) late stage (V_{inj} = 21.0 ml and d_{rel} = 16.7 mm). Panels in the second**
1000 **row show the final (cumulative deformation) stage (d_{rel} = 30 mm, V_{inj} = 37.7 ml): (d) surface image; (e) cumulative**
1001 **vertical displacement (tot. d_{rel}=30mm) and (f) cumulative shear strain (E_{xy}). Dotted circles indicate the position**
1002 **of the basal injection.**

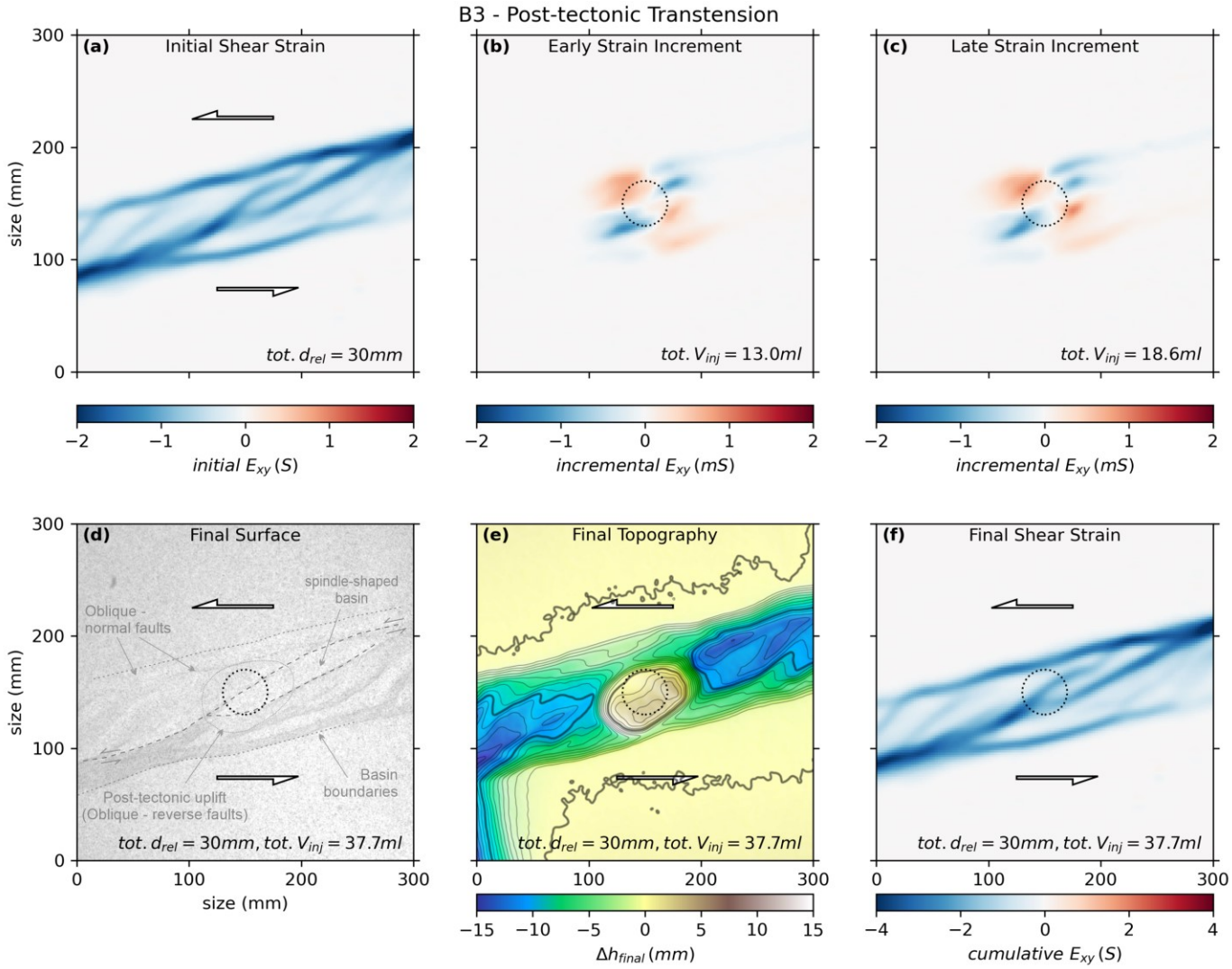

Fig. 10 Surface deformation of the post-tectonic intrusion model in transtension (Model B3). Shown are snapshots representative of the evolution: (a) Accumulated strain at the beginning of intrusion (d_{rel} = 30 mm), (b) incremental strain during an early (V_{inj} = 13 ml) and (c) late stage (V_{inj} = 18.6 ml) of intrusion. Panels in the second row show the final (cumulative deformation) stage (d_{rel} = 30 mm, V_{inj} = 37.7 ml): (d) surface image; (e) cumulative vertical displacement (tot. d_{rel}=30mm) and (f) cumulative shear strain (E_{xy}). Dotted circles indicate the position of the basal injection.

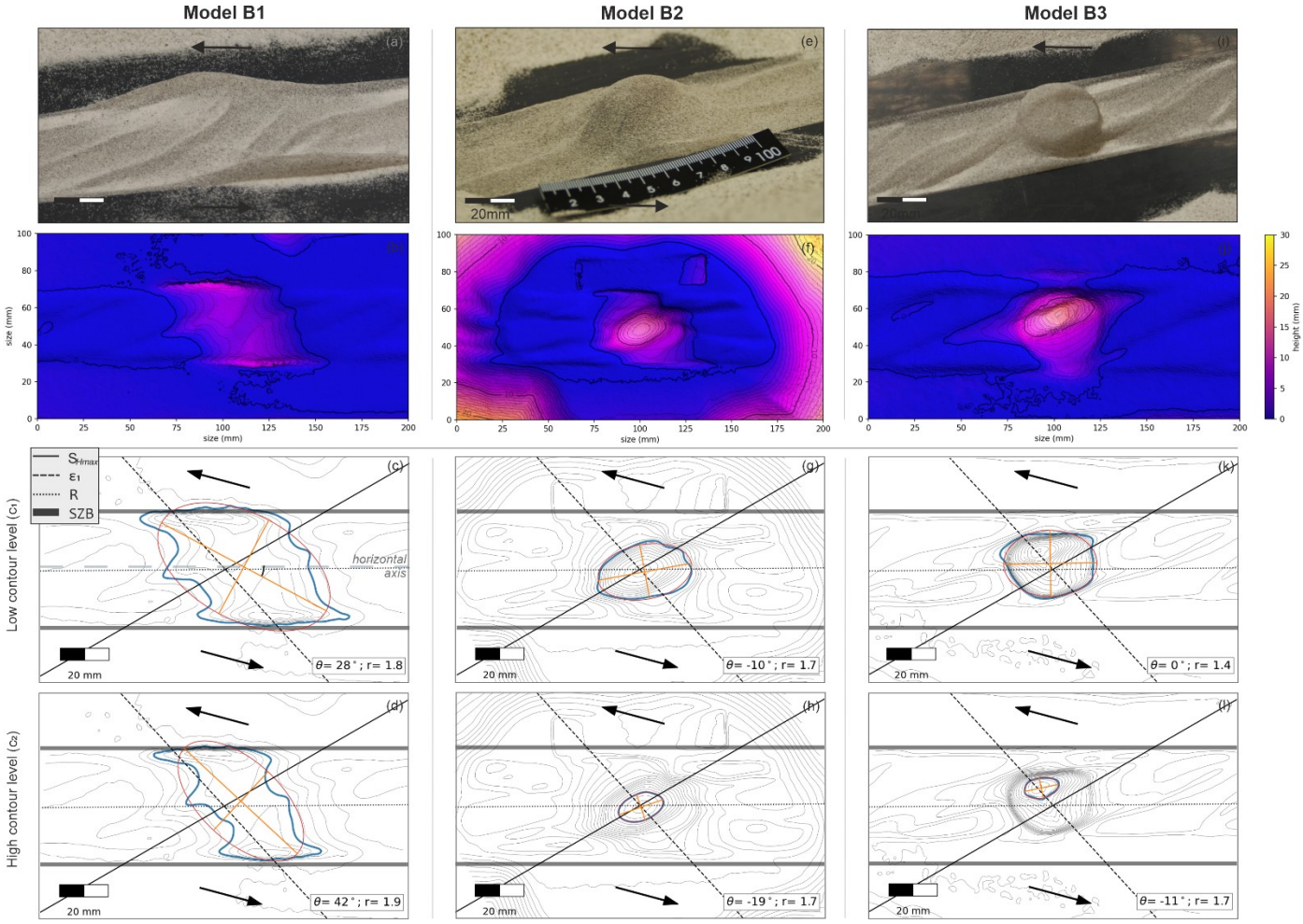

Fig. 11 Models of the intrusions in the transtensional regime (Group B): Model B1 (a-c); Model B2 (d-f) and Model B3 (g-i). (a, d, g) Oblique views of the excavated intrusions; (b, e, h) Digital Intrusion Models (DIM) coloured and with contour lines; (c, f, i) Orientation and geometry of the intrusion (in map view), where θ = the angle between the long axis (orange) of the fitted ellipse (red) and the strike of the basal shear zone. r is the intrusion's aspect ratio (length-to-width ratio, L/W). Light and dark grey quadrants indicate contraction and extensional quadrants, respectively.

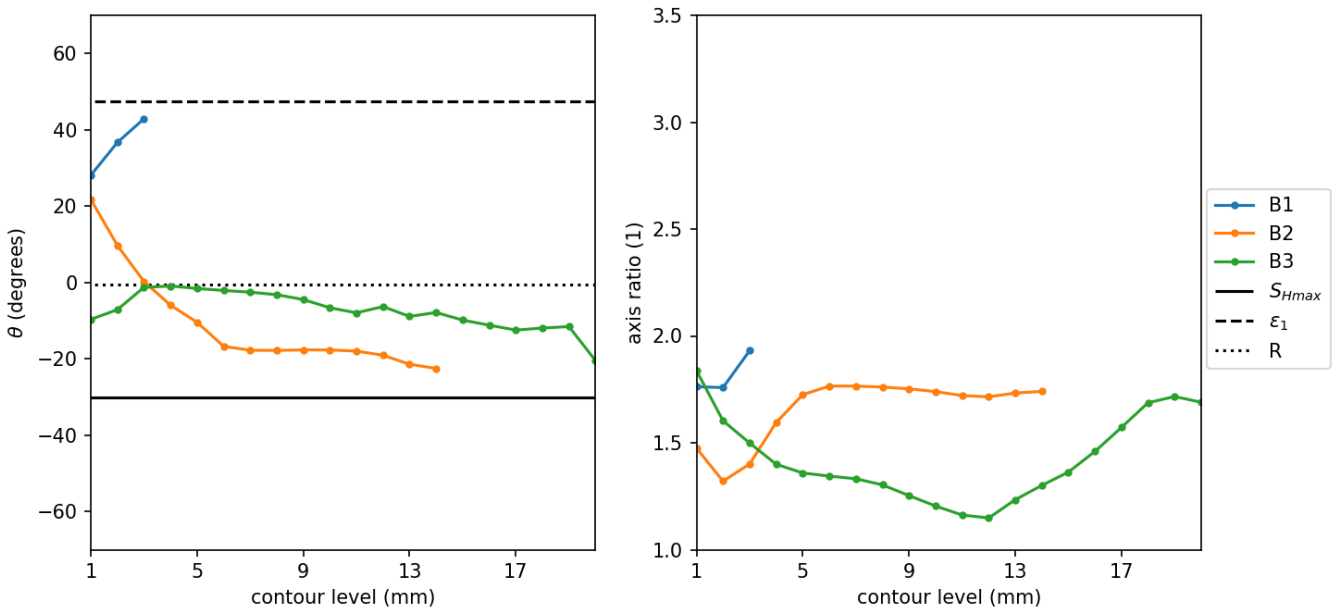

1017

1018 **Fig.12 Series B experimental results expressed in graph of angles and ratios ellipses vs. intrusion contour level.**

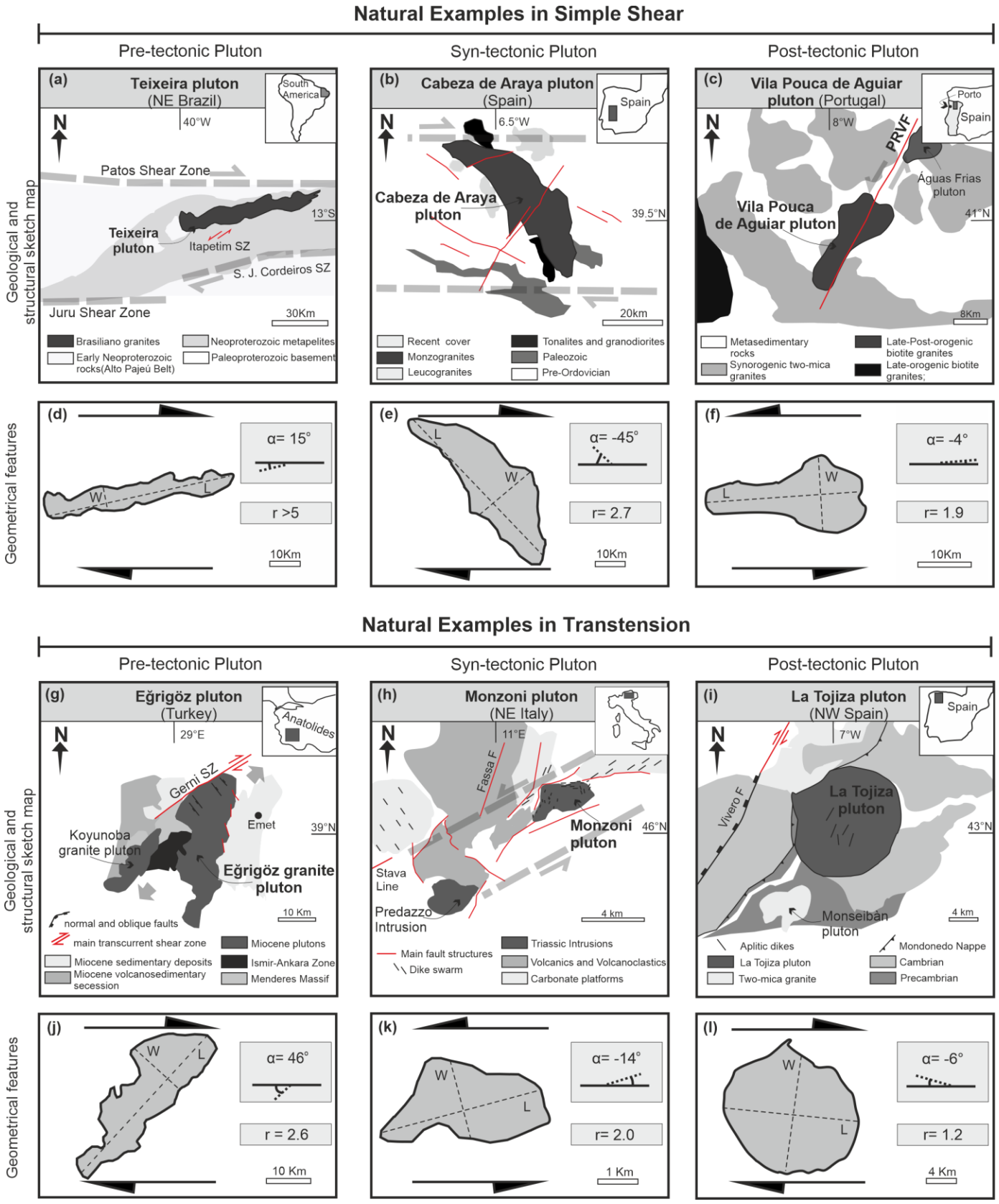

Fig. 13 Simplified geological maps and shapes of natural plutons emplaced in simple shear and transtensional zones: (a, d) The Teixeira pluton (Archanjo et al., 2008); (b, e) The Cabeza de Araya Pluton (Vigneresse and Bouchez, 1997; Fernandez and Castro, 1999; Corti et al., 2005) and (c, f) The Vila Pouca de Aguiar pluton (Sant'Ovaia et al., 2000). Plutons emplaced in transtensional regime: (g, j) The Eğrigöz pluton is a pre-tectonic

intrusion affected by rotation due to the transtensional deformation occurring after the emplacement (Erkül et al., 2017); (h, k) The Monzoni Pluton developed within a transtensional tectonic environment (Sloman, 1989; Bonadiman et al., 1994); (i, l) La Tojiza Pluton is a clear example of post-tectonic intrusion only slightly reactivating the previous transtensional tectonic structures (Aranguren et al., 2003).

9 Appendix – Supplementary data

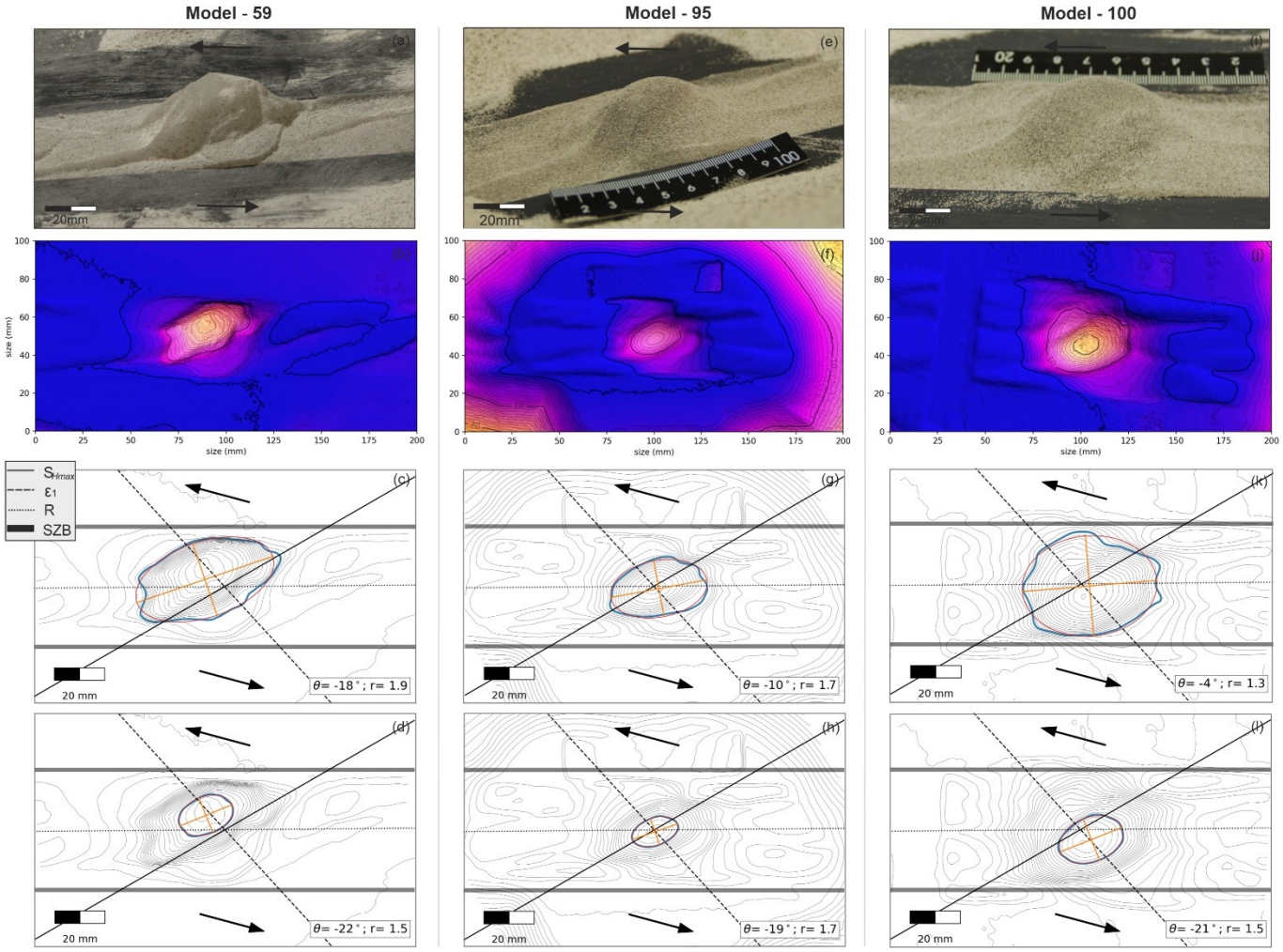

A.1 Intrinsic variability of intrusion models verified by repeating experiments (Model B2) in syn-tectonic intrusion in transtension.

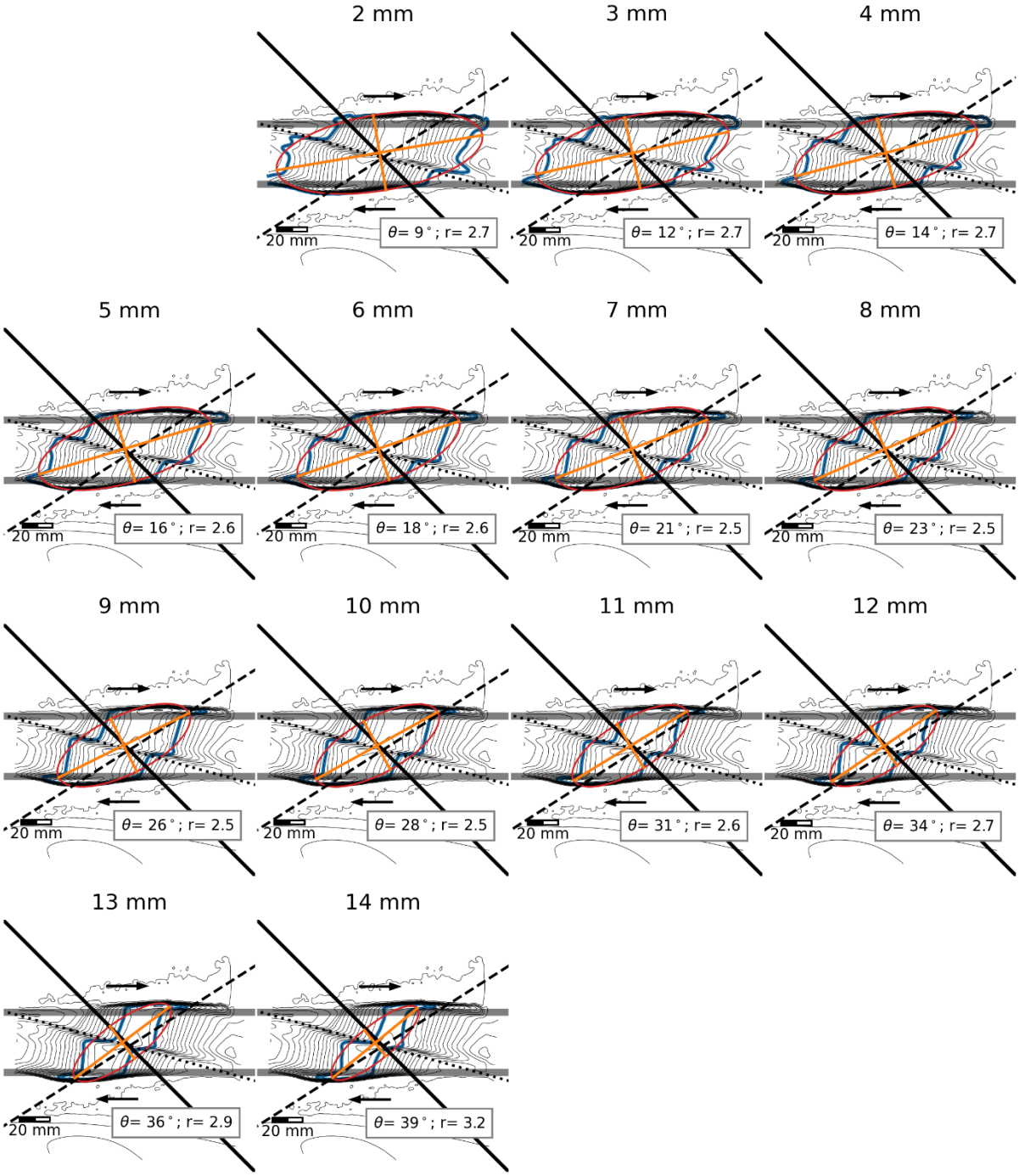

A.2 Complete contour ellipses analysis of the Model A1 shape as a function of height

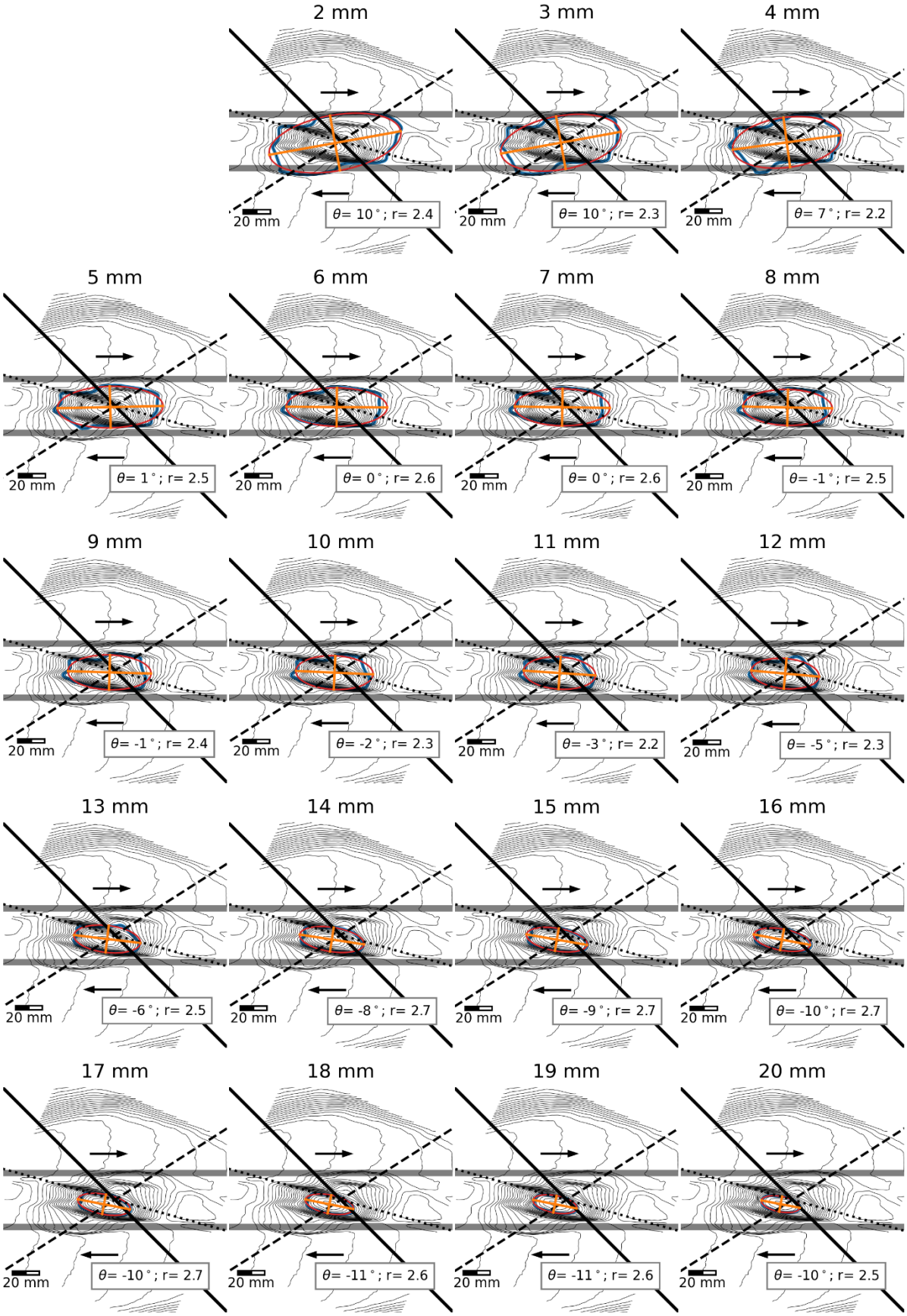

A.3 Complete contour ellipses analysis of the Model A2 shape as a function of height

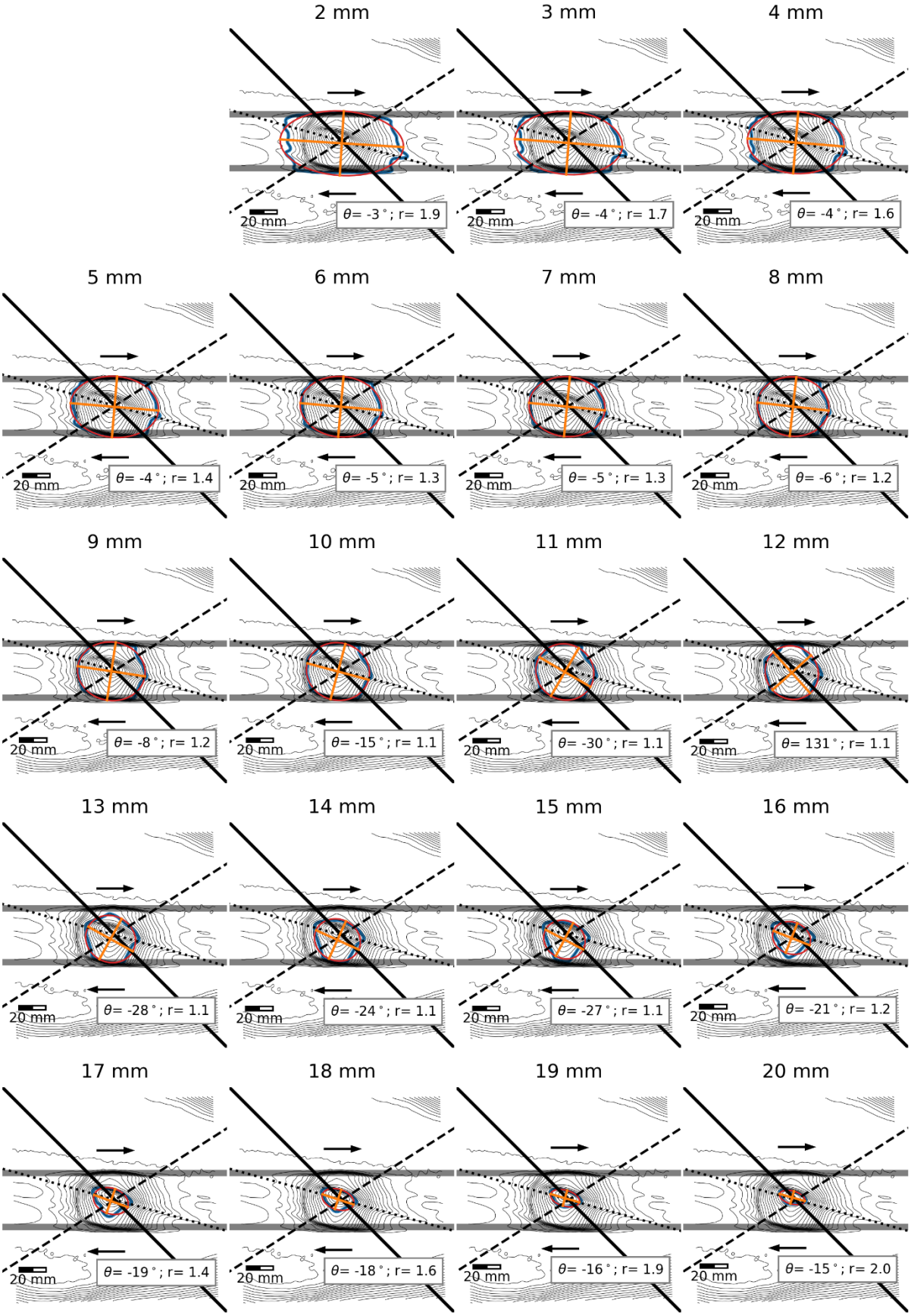

A.4 Complete contour ellipses analysis of the Model A3 shape as a function of height

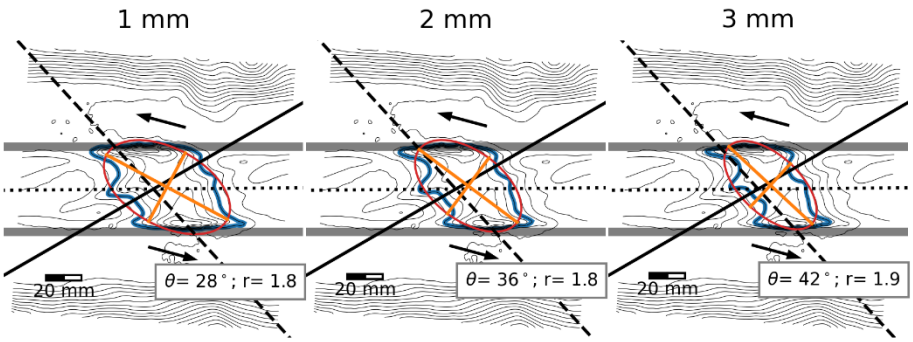

1039

1040 **A.5 Complete contour ellipses analysis of the Model B1 shape as a function of height**

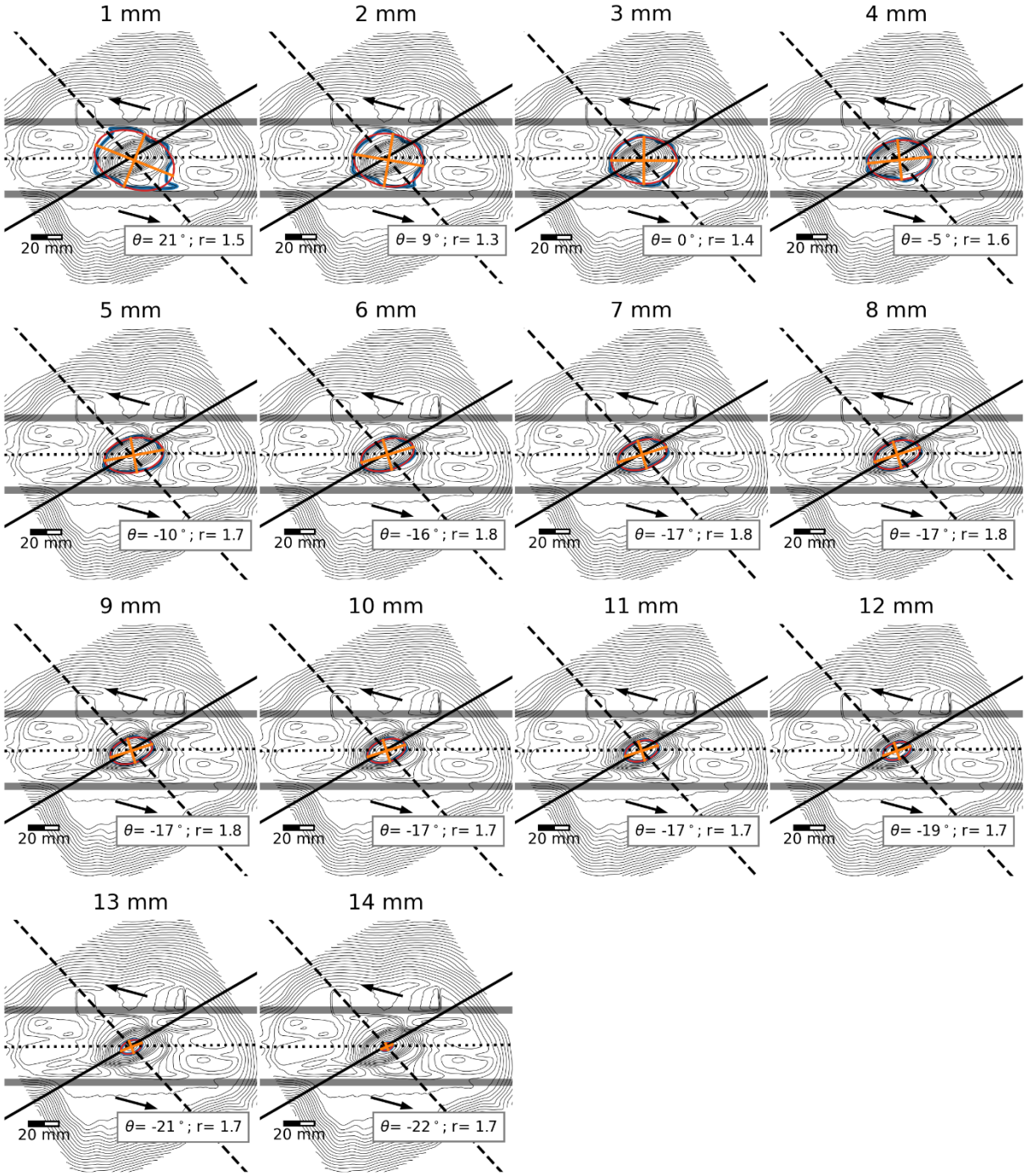

A.6 Complete contour ellipses analysis of the Model B2 shape as a function of height

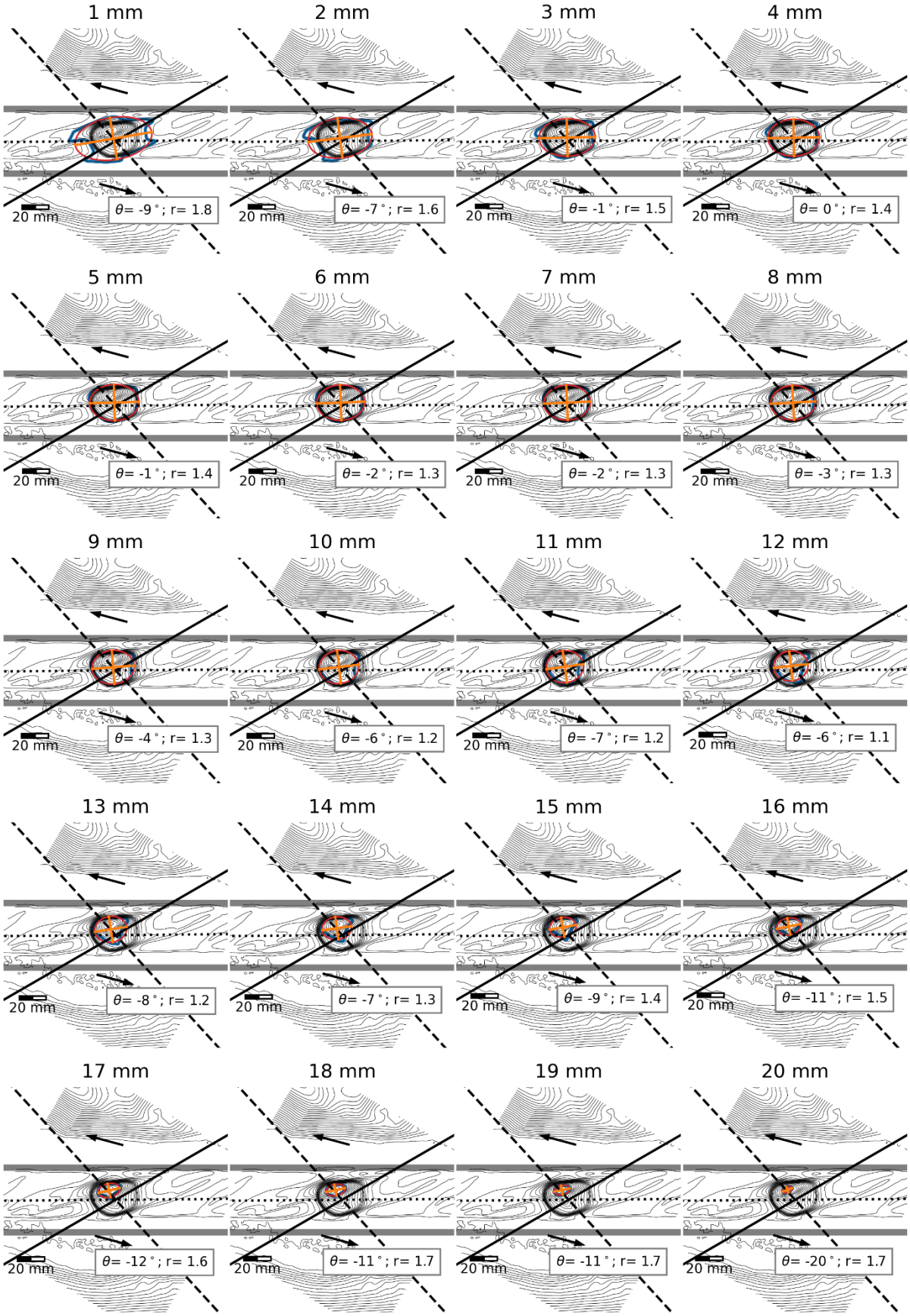

A.7 Complete contour ellipses analysis of the Model B3 shape as a function of height